



1 Adjusting particle-size distributions to account for 2 aggregation in tephra-deposit model forecasts

3

4 Larry G. Mastin¹, Alexa R. Van Eaton¹, and Adam J. Durant^{2,3}

5 [1] [U.S. Geological Survey, Cascades Volcano Observatory, 1300 SE Cardinal Court, Bldg.
6 10, Suite 100, Vancouver, Washington, USA]

7 [2] [Section for Meteorology and Oceanography, Department of Geosciences, University of
8 Oslo, Blindern, 0316 Oslo, Norway]

9 [3] [Geological and Mining Engineering and Sciences, Michigan Technological University,
10 1400 Townsend Drive, Houghton, MI 49931, USA]

11

12 Abstract

13 Volcanic ash transport and dispersion models (VATDs) are used to forecast tephra deposition
14 during volcanic eruptions. Model accuracy is limited by the fact that fine ash aggregates,
15 altering patterns of deposition. In most models this is accounted for by *ad hoc* changes to model
16 input, representing fine ash as aggregates with density ρ_{agg} , and a log-normal size distribution
17 with median μ_{agg} and standard deviation σ_{agg} . Optimal values may vary between eruptions.
18 To test the variance, we used the Ash3d tephra model to simulate four deposits: 18 May 1980
19 Mount St. Helens; 16-17 September 1992 Crater Peak (Mount Spurr); 17 June 1996 Ruapehu;
20 and 23 March 2009 Mount Redoubt. In 158 simulations, we systematically varied μ_{agg} and
21 σ_{agg} , holding ρ_{agg} constant at 600 kg m^{-3} . We evaluated the fit using three indices that compare
22 modeled versus measured (1) mass load at sample locations; (2) mass load versus distance along
23 the dispersal axis; and (3) isomass area. For all deposits, under these inputs, the best-fit value
24 of μ_{agg} ranged narrowly between $\sim 2.1\text{-}2.5\phi$ (0.23-0.18mm), despite large variations in erupted
25 mass (0.25-50Tg), plume height (8.5-25 km), mass fraction of fine (<0.063mm) ash (3-59%),
26 atmospheric temperature, and water content between these eruptions. This close agreement
27 suggests that aggregation may be treated as a discrete process that is insensitive to eruptive style
28 or magnitude. This result offers the potential for a simple, computationally-efficient



29 parameterization scheme for use in operational model forecasts. Further research may indicate
30 whether this narrow range also reflects physical constraints on processes in the evolving cloud.

31

32 **1 Introduction**

33 Airborne tephra is the most wide-reaching of volcanic hazards. It can extend hundreds to
34 thousands of kilometers from a volcano and impact air quality, transportation, crops, electrical
35 infrastructure, buildings, water supplies, and sewerage. During eruptions, communities want
36 to know whether they may receive tephra and how much might fall. Volcano observatories
37 typically forecast areas at risk by running volcanic ash transport and dispersion models
38 (VATD). As input, these models require information including eruption start time, plume
39 height, duration, the wind field, and the size distribution of the falling particles. Of these inputs,
40 the particle size distribution is perhaps the hardest to constrain.

41 Particle size (along with shape and density) determines settling velocity, which controls where
42 particles land in a given wind field. For different eruptions, the total particle-size distribution
43 (TPSD) can vary. Large eruptions produce more fine ash than small ones for example; and
44 silicic eruptions produce more than mafic (Rose and Durant, 2009). The TPSD is difficult to
45 estimate (e.g., Bonadonna and Houghton, 2005); hence estimates exist for only a handful of
46 deposits. And even in cases where the TPSD is known, that TPSD, entered into a dispersion
47 model, will not accurately calculate the pattern of deposition (Carey, 1996).

48 This inaccuracy results from the fact that complex processes, not considered in models, cause
49 particles to fall out faster than theoretical settling velocities would predict. These processes
50 include scavenging by hydrometeors (Rose et al., 1995a), gravitational instabilities that cause
51 dense clouds to collapse *en masse* (Carazzo and Jellinek, 2012; Schultz et al., 2006; Durant,
52 2015; Manzella et al., 2015), and aggregation, in which ash particles smaller than a few hundred
53 microns clump into clusters. The rate of aggregation, and the type and size of resulting
54 aggregates, depend on atmospheric processes such as ice accretion, electrostatic attraction, or
55 liquid-water binding whose importance varies from place to place.

56 Although one VATD model, Fall3d, calculates aggregation during transport for research studies
57 (Folch et al., 2010; Costa et al., 2010), no operational models consider it. Instead, aggregation
58 is accounted for by either setting a minimum settling velocity in the code (Carey and
59 Sigurdsson, 1982; Hurst and Turner, 1999; Armienti et al., 1988; Macedonio et al., 1988), or,



60 in the model input, adjusting particle size distribution by replacing some of the fine ash with
61 aggregates of a specified density, shape, and size range (Bonadonna et al., 2002; Cornell et al.,
62 1983; Mastin et al., 2013b). These strategies will probably prevail for at least the next few
63 years, until microphysical algorithms replace them.

64 These adjustments are mostly derived from *a posteriori* studies, where model inputs have been
65 adjusted until results match a particular deposit. It is unclear how well the optimal adjustments
66 might vary from case to case. For model forecasts during an eruption, we need some
67 understanding of this variability. This paper addresses this question, using deposits from four
68 well-documented eruptions. We derive a scheme for adjusting TPSD to account for
69 aggregation, optimize parameter values to match each deposit, and then see how much these
70 optimal values vary from one deposit to the next.

71 **2 Background on the deposits**

72 The IAVCEI Commission on Tephra Hazard Modeling has posted data from eight well-mapped
73 eruption deposits, available for use by modeling groups to validate VATD simulations
74 (<http://dbstr.ct.ingv.it/iaucei/>). Of these, we focus on eruptions that lasted for hours (not days);
75 where the TPSD included at least a few percent of ash finer than 0.063mm in diameter; and
76 where data were available from distal (>35 km) sample locations. Four eruptions met these
77 criteria: the 18 May 1980 eruption of Mount St. Helens, 16-17 June 1996 eruption of Ruapehu,
78 and the 16-17 September and 18 August 1992 eruptions of Crater Peak (Mount Spurr), Alaska.
79 The August Crater Peak eruption was already studied using Ash3d (Schwaiger et al., 2012) and
80 therefore not included here, reducing the total to three. To these we add event 5 from the 23
81 March 2009 eruption of Mount Redoubt, Alaska. Although an Ash3d study was made of this
82 event (Mastin et al., 2013b), aggregation has been unusually well characterized in recent years
83 (Wallace et al., 2013; Van Eaton et al., in press).

84 Below are key observations of these events. Deposit maps are shown in Fig. 1, digitized from
85 published sources.

86 **1) The 18 May 1980 deposit from Mount St. Helens** remains among the best documented of
87 any in recent decades (Durant et al., 2009; Sarna-Wojcicki et al., 1981; Waitt and Dzurisin,
88 1981; Rice, 1981). This 9 hour eruption expelled magma that was dacitic in bulk composition
89 but contained about 40% crystals and 60% rhyolitic glass (Rutherford et al., 1985). The
90 eruption start time (1532 UTC) and duration are well documented (Foxworthy and Hill, 1982);
91 the time-changing plume height was tracked by Doppler radar (Harris et al., 1981) and satellite



92 (Holasek and Self, 1995) (Table 2). The deposit was mapped within days, before modification
93 by wind or rainfall, to a distance of ~800 km and to mass load values as low as a few hundredths
94 of a kilogram per square meter (Sarna-Wojcicki et al., 1981). Estimated volume of the fall
95 deposit in dense-rock equivalent (DRE) is 0.2 km^3 (Sarna-Wojcicki et al., 1981) based on what
96 fell in the mapped area. A TPSD was estimated by Carey and Sigurdsson (1982) and later by
97 Durant et al. (2009) to contain about 59% ash <63 μm in diameter (Table S1), with a modal
98 peak in particle size that coincided with the median bubble size of tephra fragments (Genareau
99 et al., 2012). Some fine ash may have been milled in pyroclastic density currents on the
100 afternoon of 18 May and in the lateral blast that morning. A secondary maximum in deposit
101 thickness in Ritzville, Washington (~290 km downwind) was inferred by Carey and Sigurdsson
102 (1982) to have resulted from fine ash aggregating and falling *en masse*, perhaps as the cloud
103 descended and warmed to above-freezing temperatures (Durant et al., 2009). Wind directions
104 that were more southerly at low elevations combined with elutriation off pyroclastic flows in
105 the afternoon to feed low clouds, producing a deposit that was richer in fine ash along its
106 northern boundary than in the south (Waitt and Dzurisin, 1981; Eychenne et al., 2015).
107 Aggregates sampled by Sorem (1982) in eastern Washington consisted mainly of dry clusters
108 0.250 to 0.500 mm in diameter, containing particles <0.001mm to more than 0.040mm in
109 diameter, though no aggregates were visible in the fall deposit except at proximal locations (e.g.
110 Sisson (1995)). The eruption began under clear weather conditions. Clouds increased
111 throughout the day. Some precipitation in the form of mud rain was noted within tens of
112 kilometers of the vent (Rosenbaum and Waitt, 1981), probably due to entrainment and
113 condensation of atmospheric moisture in the rising plume. But no precipitation was recorded
114 at more distal locations during the event.

115 **2) The 16-17 September 1991 eruption from Crater Peak, Mount Spurr, Alaska**, was the
116 third that summer from this vent. The eruption start time (0803 UTC September 17) and
117 duration (3.6 hours (Eichelberger et al., 1995)) were seismically constrained. The maximum
118 plume height, measured by U.S. National Weather Service radar (Rose et al., 1995b) increased
119 for the first 2.3 hours and then fluctuated between about 11 and 14 km above mean sea level
120 (MSL) until the plume height abruptly decreased at 1110 UTC. The andesitic tephra consisted
121 of two main types; tan and gray, which were both noteworthy for their low vesicularity (~20-
122 45%) and high crystallinity (40-100%) (Gardner et al., 1998). The deposit was mapped rapidly
123 after the eruption (Neal et al., 1995; McGimsey et al., 2001) to a distance of 380 km and mass
124 loads around 0.050 kg m^{-2} . This deposit displays a weak secondary thickness maximum 260-



125 330 km downwind. Durant and Rose (2009) derived a TPSD for this deposit, estimating about
126 40% smaller than 0.063 mm. Milling in proximal pyroclastic flows that accompanied this
127 eruption (Eichelberger et al., 1995) could have contributed fine ash. The eruption occurred at
128 night under clear skies (Neal et al., 1995).

129 **3) The 17 June 1996 eruption of Ruapehu** produced a classic weak plume that was modeled
130 by Bonadonna et al. (2005), Hurst and Turner (1999), Scollo et al. (2008), Liu et al. (2015), and
131 Klawonn et al. (2014), among others. The main phase involved two pulses, one beginning 16
132 June at 1910 UTC and lasting 2.5 hours, and the second at 2300 UTC and lasting approximately
133 1.5 to 2 hours. Ash-laden plumes reached to about 8.5 km altitude above MSL based on satellite
134 infrared images (Prata and Grant, 2001). The deposit was mapped out to the Bay of Plenty
135 (190 km), sampled at 118 locations to mass loads less than 0.01 kg m⁻², and yielded a total mass
136 of about 0.001 km³ DRE (Bonadonna and Houghton, 2005). Ejecta consisted mainly of scoria
137 containing 75% glass and 25% crystals, with glass containing about 54 wt% SiO₂ (Nakagawa
138 et al., 1999). A TPSD estimate based on the Voronoi tessellation method (Bonadonna and
139 Houghton, 2005) suggested that ash <0.063 mm composed only about 3% of the deposit. A
140 minor secondary thickness maximum was constrained by mapping at about 160 km downwind
141 (Bonadonna et al., 2005) (Fig. 1c). Although some witnesses at distal locations observed loose,
142 millimeter-sized clusters falling, no aggregates or accretionary lapilli were present in the
143 deposit (Klawonn et al., 2014). The eruption was not accompanied by significant pyroclastic
144 density currents and occurred during clear weather.

145 **4) Event 5 of the 23 March 2009 eruption of Redoubt Volcano, Alaska** erupted through a
146 glacier and entrained a variable amount of water into a high-latitude early-spring atmosphere.
147 It began at 1230 UTC, lasted about 20 minutes on the seismic record (Buurman et al., 2013),
148 and sent a plume briefly to about 18 km as seen in both National Weather Service NEXRAD
149 Doppler radar from Anchorage, and a USGS mobile C-band radar system in Kenai, Alaska
150 (Schneider and Hoblitt, 2013). Within a few days after the eruption, the deposit was mapped
151 by its contrast with underlying snow in satellite images (NASA MODIS), and sampled for mass
152 load and particle size distribution at 38 locations, at distances up to ~250 km and mass loads as
153 low as 0.01 kg m⁻² (Wallace et al., 2013). During Ash3d modeling of this eruption, Mastin et
154 al. (2013b) found that wind vectors varied rapidly with both altitude and time, making the
155 dispersal direction highly sensitive to both the plume height (which varied from ~12 to 18 km
156 during the 20-minute eruption) and the vertical distribution of mass in the plume. In the deposit,



157 Wallace et al. (2013) described abundant frozen aggregates with size decreasing with distance
158 from the vent, from about 10mm at 12 km distance. Schneider et al. (2013) attributed the high
159 (>50 dBZ) reflectivity of the proximal plume in radar images, and a rapid decrease in maximum
160 plume height over a period of minutes, to formation and fallout of ashy hail hydrometeors in
161 the rising column. Van Eaton et al. (2015) combined analysis of the aggregate microstructures
162 with a 3-D large-eddy simulation to show that the ash aggregates grew directly within the
163 volcanic plume from a combination of wet growth and freezing, in a process similar to hail
164 formation.

165 These eruptions vary from weak (Ruapehu) to strong (Redoubt) plumes, from mid-latitude (St.
166 Helens, Ruapehu) to high-latitude (Spurr, Redoubt), from dry (Ruapehu) to relatively wet
167 (Redoubt), from basaltic andesite (Ruapehu) to dacite (St. Helens), and from ~3% to 59% ash
168 <0.063 mm in diameter. Inferred aggregation processes range from dry (Ruapehu) to wet within
169 the downwind cloud (St. Helens), to liquid+ice in the rising column (Redoubt).

170 **3 Methods**

171 **3.1 The Ash3d model**

172 We model these eruptions using Ash3d (Schwaiger et al., 2012; Mastin et al., 2013a), an
173 Eulerian model that calculates tephra transport and deposition through a 3-D, time-changing
174 wind field. Ash3d calculates transport by setting up a three dimensional grid of cells, adding
175 tephra into the column of source cells above the volcano, and distributing the mass in the
176 column following the Suzuki relation (Suzuki, 1983),

$$177 \quad \frac{dQ_m}{dz} = Q_m \frac{k^2 (1 - z/H_v) \exp(k(z/H_v - 1))}{H_v [1 - (1 + k) \exp(-k)]}, \quad (1)$$

178 where Q_m is the mass eruption rate, H_v is plume height above the vent, z is elevation (above the
179 vent) within the plume, and k is a constant that adjusts the mass distribution.

180 At each time step, tephra transport is calculated through advection by wind, through turbulent
181 diffusion, and through particle settling. For wind advection, simulations of Mount St. Helens,
182 Crater Peak, and Redoubt use a wind field obtained from the National Oceanic and Atmospheric
183 Administration's (NOAA's) NCEP/NCAR Reanalysis 1 model ("RE1") (Kalnay et al., 1996).
184 For the Ruapehu simulations we used a local 1-D wind sounding, which gave more accurate
185 results. The RE1 model provides wind vectors on a global 3-D grid spaced at 2.5° latitude and



186 longitude, and 17 pressure levels in the atmosphere (1000-10 hPa), updated at 6-hour intervals.
187 Ash3d calculates turbulent diffusion using a specified diffusivity D (Schwaiger et al., 2012, eq.
188 4). D is set to zero for simplicity, though later we show the effect of different values of D .

189 Settling rates are calculated using relations of Wilson and Huang (1979) for ellipsoidal particles.
190 Wilson and Huang define a particle shape factor $F \equiv (b + c)/2a$, where a , b , and c are the semi-
191 major, intermediate, and semi-minor axes of the ellipsoid respectively. Wilson and Huang
192 measured a , b , and c for 155 natural pyroclasts. The average F of their measurements was 0.44,
193 which we use in our model. For aggregates we use $F=1.0$ (round aggregates).

194 Other model inputs include the extent and nodal spacing of the model domain; vent location
195 and elevation; the eruption start time, duration, plume height, erupted volume, diffusion
196 coefficient D , and a series of particle size classes and associated densities. The size classes
197 may represent either individual particles or aggregates. These input values are given in Tables
198 1 and 2.

199 **3.2 Adjusting particle size distributions to account for aggregation**

200 The TPSD used to model these four eruptions are listed in Table S1 and illustrated in Fig. 2.
201 We aim to adjust the TPSD in our model to better match the mapped deposits. In doing so, we
202 assume that some fraction (m_{agg}) of ash smaller than some size ϕ_p^{max} collects into clusters having
203 a density ρ_{agg} and Gaussian size distribution of mean μ_{agg} , and standard deviation σ_{agg} . For
204 deposit modeling, we ignore the small fraction of the erupted mass that goes into the distal
205 cloud, typically a few percent (Dacre et al., 2011; Devenish et al., 2012). In the Appendix we
206 briefly review aggregation processes. We offer the following parameterization scheme:

207 For $\phi \geq 4$, all ash aggregates

208 For $\phi \leq 2$, no ash aggregates.

209 For $4 > \phi > 2$, the mass fraction that aggregates varies linearly with ϕ from 1 (when $\phi=4$) to 0
210 (when $\phi=2$).

211 Based on this scheme, particle sizes that aggregate are depicted as gray bars in Fig. 2.



212 3.3 Statistical measures of fit

213 For each eruption, we have done a series of model simulations, first using the TPSD without
214 considering aggregation, and then systematically varying σ_{agg} and μ_{agg} to include the effects of
215 aggregation. We compare the resulting deposit with the mapped deposit using three methods
216 presented in Table 3. Each has advantages and disadvantages.

217 1) **The point-by-point index** Δ^2 compares model results with sample data collected at specific
218 locations (dots, Fig. 1). It offers the advantage that the comparison is made directly with
219 measured values, not with interpreted or extrapolated contours of data. But Δ^2 values are
220 dominated by differences in proximal locations where mass per unit area is greatest; and values
221 of Δ^2 can be influenced by errors in the wind field, which cannot be adjusted in the model.

222 2) **The downwind thinning index** $\Delta_{downwind}^2$, compares modeled mass per unit area along the
223 downwind dispersal axis with values expected at that distance based on a trend line drawn from
224 field measurements (Fig. 3). The comparison is not made directly with measured values (a
225 disadvantage). However the method does not suffer the limitation of over-weighting proximal
226 data. And, more importantly, it still provides a useful comparison when wind errors cause the
227 modeled dispersal axis to diverge from the mapped one.

228 3) **The isomass area index** Δ_{area}^2 compares the area within modeled and mapped isomass
229 lines. It is based on traditional plots of the log of isopach thickness versus square root of area
230 (Pyle, 1989; Fierstein and Nathenson, 1992; Bonadonna and Costa, 2012), which are assumed
231 to accurately depict the areal distribution of tephra while minimizing the effects of 3-D wind
232 on the distribution (Pyle, 1989). Fig. 4 shows plots for our four eruptions, using the log of
233 isomass rather than isopach thickness to avoid problems introduced by varying deposit density.

234 The index Δ_{area}^2 is assumed to be insensitive to effects of wind (an advantage). However,
235 model results are compared with isopach lines that are interpretive and may not be well
236 constrained, depending on the distribution and number density of sample locations.

237 3.4 Sensitivity to various input values

238 We ignore complex, proximal fallout and concentrate on medial to distal areas, about 100 to
239 ~500 km downwind for example at Mount St. Helens. There, under the average wind speed
240 (15.1 m s^{-1}) that existed below about 15 km, tephra falling from 15km at average settling



241 velocities of $0.4\text{--}1.5\text{ m s}^{-1}$ would deposit within this range (Fig. 5a). Tephra falling at $0.66\text{--}0.78$
242 m s^{-1} would land 290–340 km downwind, the distance of the secondary maximum at Ritzville.
243 A wide range of aggregate diameters d could fall at this rate depending on density ρ_{agg} (Fig.
244 5b). For simplicity, we hold ρ_{agg} constant at 600 kg m^{-3} , toward the middle of the observed
245 range of aggregate densities ($\sim 50\text{--}1600\text{ kg m}^{-3}$ (Sparks et al., 1997, Table 16.1; Taddeucci et
246 al., 2011)).

247 Other factors listed below can also affect the results.

248 **Aggregate shape.** Aggregate shape can strongly affect the settling velocity and thus where
249 deposits fall, as illustrated in Fig. 6. For simplicity, we use round aggregates ($F=1.0$).

250 **Suzuki k .** Simulations of Mount St. Helens (Fig. 7) show that increasing the Suzuki factor from
251 4 to 8 increases the prominence of a secondary thickness maximum. But at $k>\sim 8$, the proximal
252 deposit becomes unrealistically thin. Our simulations use $k=8$ to replicate the known prominent
253 secondary thickening while minimizing unrealistic thinning of proximal deposits.

254 **Aggregate size.** The transport distance is highly sensitive to aggregate size. Reducing
255 aggregate diameter d from 0.250 to 0.217 to 0.189 mm increases transport distance at Mount
256 St. Helens from 300 to 366 to 448 km respectively (Fig. 5a). In simulations that use a single,
257 dominant aggregate size, these variations produce conspicuous changes in the location of a
258 secondary maximum (Fig. 8). Decreasing size also decreases the percent of erupted mass lands
259 in the mapped area: from 70% to 53% to 39% for $d=0.165, 0.143,$ and 0.125mm respectively.
260 Our simulations limit μ_{agg} to values of $1.8\text{--}3.1\phi$ ($0.287\text{--}0.117\text{mm}$), and σ_{agg} to $0.1\text{--}0.3\phi$, to
261 ensure that most deposits fall in the region of interest.

262

263 4 Results

264 We ran simulations at $\mu_{agg}=1.8, 1.9, 2.0 \dots 3.1\phi$, and $\sigma_{agg} 0.1, 0.2,$ and 0.3ϕ . The latter used
265 1, 3, and 5 aggregate size classes respectively, in each simulation, with the percentage of fine
266 ash assigned to each bin given in Table 4. Our calculations of Δ^2 and $\Delta_{downwind}^2$ only included
267 sample points whose downwind distance lay within the range indicated by the trend lines in
268 Fig. 3.



269 Figure 9 shows contours of Δ^2 , $\Delta_{downwind}^2$, and Δ_{area}^2 as a function of σ_{agg} and μ_{agg} for each of
270 these four deposits. Values are given in Tables S3-S6. Although the three indices compare
271 different features of the deposit, they provide roughly similar optimal values of σ_{agg} and μ_{agg} .
272 For Mount St. Helens, for example, the best-fit value of μ_{agg} is about 2.3ϕ using Δ^2 (Fig. 9a),
273 2.5ϕ using $\Delta_{downwind}^2$ (Fig. 9b), and 2.6ϕ using Δ_{area}^2 (Fig. 9c). The fit does not depend very
274 strongly on σ_{agg} but appears slightly better at higher values. For Crater Peak, optimal μ_{agg}
275 values are 2.3ϕ , 2.2ϕ , and 1.9ϕ respectively. For Ruapehu they are about 2.1 - 2.4ϕ (poorly
276 constrained), 2.2ϕ , and 2.3ϕ . For both Crater Peak and Ruapehu, the fit is also insensitive to
277 σ_{agg} , though slightly better at higher values for Ruapehu using Δ_{area}^2 (Fig. 9i). For Redoubt,
278 optimal values are disparate: $\mu_{agg} = 2.1$ - 2.2ϕ , 2.3ϕ , and $<1\phi$ respectively. The Redoubt deposit
279 is least constrained by field data and the most difficult to match due to the complex wind
280 conditions.

281 Figures 10-13 show results for each of these eruptions using $\mu_{agg} = 2.4\phi$ (0.29mm) and σ_{agg}
282 $= 0.3\phi$. The sizes of particles and aggregates used to generate these figures is given in Table
283 S2. For all deposits these values are close to optimal, depending on which criterion is used.
284 Similar figures for other values of μ_{agg} and σ_{agg} are provided as Figs. S005-S172.

285 Figures S001-S004 show simulations using the original particle-size distribution, with no
286 aggregation. Tephra fall beyond a few tens of kilometers is strongly underestimated in all these
287 runs, especially for the three eruptions that contain more than a few percent fine ash. Values
288 of Δ^2 , $\Delta_{downwind}^2$, and Δ_{area}^2 are also higher than most simulations that use aggregates (Table S3-
289 S6). For Mount St. Helens, Crater Peak, Ruapehu, and Redoubt, the percentages of the erupted
290 mass landing in the mapped area are very low: 29%, 42%, 88%, and 59% respectively.

291 Optimal aggregates obtained from our study are similar in size but denser than those found
292 optimal by Cornell et al. (1983) for the Campanian Y-5 ($\mu_{agg} = 2.3\phi$, $\rho_{agg} = 200 \text{ kg m}^{-3}$). The
293 unknown wind field during the prehistoric Campanian Y-5 eruption makes it difficult to
294 compare Cornell et al.'s optimal value to the results here. Folch et al. (2010) matched the
295 Mount St. Helens deposit using a similar aggregation scheme, but with aggregates of density



296 400 kg m⁻³ (compared with our 600 kg m⁻³) and diameter of 0.2-0.3mm (compared with our
297 ~0.2mm). Their results are broadly consistent with ours.

298 **4.1 Mount St. Helens**

299 For the Mount St. Helens case, the modeled deposit follows a dispersal axis (solid black line,
300 Fig. 10a) that matches almost exactly with the mapped one (dashed line). The agreement
301 reflects both the faithfulness of the numerical wind field to the true one and the appropriateness
302 of other inputs, such *k*, that influence dispersal direction. The measured mass loads in Fig. 10a,
303 indicated by the color of markers, agree reasonably well with modeled mass loads indicated by
304 colors of the contour lines, except along the most distal transect, where modeled loads are
305 essentially zero while measured loads are about 10⁻¹ kg m⁻². Figure 10b shows that modeled
306 and measured mass loads generally agree within a factor of three or so, except for those same
307 distal, low-mass-load measurements, to the lower left of the legend label (those where modeled
308 values are truly zero do not show up on this plot). Figure 10c shows that the modeled mass
309 load (black line with dots) contains a secondary thickening at about the same location mapped
310 (dashed line). However, the modeled mass load is consistently less than measured, especially
311 at the most distal sites. In Figure 10d, the log of modeled mass load versus square root of area
312 shows reasonable agreement with mapped values until mass loads are less than about 1 kg m⁻²,
313 where they diverge.

314 Notably, modeled mass loads somewhat underestimate the measured values along the dispersal
315 axis in Fig. 10c. The underestimate reflects the fact that the input erupted volume of 0.2 km³
316 DRE (Table 1) was based on estimates by Sarna-Wojcicki et al. (1981) of what lay within the
317 mapped area in Fig. 10a; yet only about 79% of the modeled mass landed within this area.
318 Reducing the mean aggregate size to 2.7φ (0.153mm, Figs. S032-S034) improves the fit
319 somewhat along distal transect near the dispersal axis but not along the entire transect length.
320 And the finer size moves the secondary maximum too far east and reduces the percentage
321 deposited to 50-60%.

322 In Fig. 10a, the modeled deposit is also narrower than the mapped one. Adding turbulent
323 diffusion, with a diffusivity *D* of about 3×10² m² s⁻¹ (Fig. 14) visually improves the fit, and was
324 likely important during this eruption due to high crosswind speeds that increased entrainment
325 (Degruyter and Bonadonna, 2012; Mastin, 2014). Ignoring turbulent diffusion decreases run



326 time by $\sim 3x$, from ~ 30 to 10 minutes for operational runs, and is a reasonable compromise
327 under operational conditions.

328 **4.2 Crater Peak (Mount Spurr)**

329 At Crater Peak (Mount Spurr), results in Fig. 11a also show good agreement between the
330 modeled dispersal axis and the mapped one (which is constrained by fewer sample locations
331 than the Mount St. Helens case). The isomass lines in this plot are jagged and irregular due to
332 effects of topography in this mountainous region. The modeled location of secondary
333 thickening in Fig. 11c agrees with the mapped location, about 250-300km downwind. Although
334 Fig. 11c shows a tendency to underestimate the mass load along the dispersal axis, there is less
335 tendency to underestimate mass load in the most distal locations as occurred at Mount St.
336 Helens. In Fig. 11d, the areas covered by modeled isomass lines are comparable to the mapped
337 values, down to mass loads approaching 0.1 kg m^{-2} .

338 **4.3 Ruapehu**

339 For Ruapehu (Fig. 12), simulations using the NCEP Reanalysis 1 numerical winds produced an
340 odd double dispersal axis whose average did not correspond well with the mapped direction of
341 dispersal (Fig. 1c). To improve the fit we used the 1-D wind sounding provided for this eruption
342 at the IAVCEI Tephra Hazard Modeling Commission web page (<http://dbstr.ct.ingv.it/iavcei/>).
343 Use of a 1-D wind sounding seems justified in this case because this deposit covers a smaller
344 area than the others, making a 3-D wind field less important in calculating transport. The
345 resulting dispersal axis (Fig. 12a) agrees with the mapped one out to about 140 km distance,
346 beyond which it strays eastward, reaching the coast, 180 km downwind, about 10 km east of
347 the mapped axis. This slight difference is enough to cause misfits in point-to-point comparisons
348 at measured mass loads of $\sim 10^{-1} \text{ kg m}^{-2}$ (Fig. 12b).

349 The modeled mass load along the dispersal axis (Fig. 12c) agrees with measurements to about
350 60-90 km distance. At 100-200 km, modeled values level off and show a hint of secondary
351 thickening at ~ 180 km, in agreement with the mapped deposit (Fig. 1c and 11c), although the
352 mapped secondary thickening is more prominent.

353 A large discrepancy is also apparent at distances of less than 60 km, where mass load along the
354 dispersal axis (Fig. 12c) and the area covered by thick isomass lines (Fig. 12d) is greater than
355 the mapped deposit. The implication is that too much mass is dropping out proximally in the



356 model. Underestimates of isomass area at $\leq 10^{-1} \text{ kg m}^{-2}$ (Fig. 12d) also show that too little is
357 falling distally. Simulations (not shown) that raise the plume height or increase k to concentrate
358 more mass high in the plume do not improve the fit. The discrepancy may reflect the coarse
359 TPSD—50% of which is coarser than 1mm (compared with 2%, 12%, and 8% for the other
360 three deposits in Table S1). An additional simulation used the TPSD derived from technique
361 B of Bonadonna and Houghton (2005) (Table S1), which divides the deposit into arbitrary
362 sectors, and calculates a weighted sum of the size distributions in each sector following Carey
363 and Sigurdsson (1982). Technique B yields a finer average particle size than technique C,
364 which uses Voronoi tessellation to sectorize the deposit. But the finer particle size of the
365 technique B TPSD does not improve the fit (Fig. S173). Further exploration of this discrepancy
366 is beyond the scope of this paper; but other possible causes could include release of different
367 particle sizes at different elevations, or complex transport in the bending of the weak plume that
368 can't be accommodated in this model.

369 A second, smaller discrepancy is that the modeled deposit is narrower than the mapped one
370 (Fig. 1c). As at Mount St. Helens, deposit widening due to cross flow entrainment is likely.
371 Increases in entrainment resulting from crossflow is widely known to both increase plume width
372 and decrease its height for a given eruption rate (Briggs, 1984; Hoult and Weil, 1972; Hewett
373 et al., 1971; Woodhouse et al., 2013). Adding turbulent diffusion, we get a visually improved
374 fit when $D \sim 3 \times 10^3 \text{ m}^2 \text{ s}^{-1}$ (Fig. 15), consistent with findings by Bonadonna et al. (2005) based
375 on the rate of downwind widening of isomass lines. This diffusivity is also similar to the visual
376 best-fit value for Mount St. Helens (Fig. 14).

377 Despite the uncertainty in TPSD, simulations that systematically vary μ_{agg} and σ_{agg} fit best in
378 Figs. 9g, h, and i when μ_{agg} is about 2.2 to 2.4. Results similar to those presented in Fig. 12c
379 use other values of μ_{agg} (Figs. S089-S130) and show a secondary maximum migrating
380 downwind as μ_{agg} increases, coming into agreement with the mapped distance at $\mu_{agg} = 2.2$ to
381 2.4ϕ (0.19-0.22mm), where errors in Fig. 9g, h, and i are lowest.

382 4.4 Redoubt

383 This deposit is the second smallest in our group, the least well-constrained by sampling, and
384 the only one in our group not known to include a secondary thickness maximum. Mastin et al.
385 (2013b) modeled this deposit using numerical winds from the North American Regional



386 Reanalysis model (Mesinger et al., 2006). During that eruption, the winds at 0-4 km, 6-10, and
387 >10 km elevation were directed toward the northwest; north, and northeast respectively, with
388 the highest speeds at 6-10 km. Mastin et al. found that the modeled cloud developed a north-
389 oriented, northward migrating wishbone shape with the west prong at low elevation and the east
390 prong at high elevation. Mastin et al. also found that the modeled dispersal axis and the mass
391 load distribution roughly agreed with mapped values for a plume height of 15km, $k=8$, and a
392 particle size adjustment that involved taking 95% of the fine ash (<0.063mm) and distributing
393 it evenly among the coarser bins. In this study we use the same plume height and k value, a
394 different wind field (RE1), and explore a different parameterization for particle aggregation.

395 In Fig. 13a, the modeled dispersal axis diverges about 20° westward from the mapped axis. We
396 do not correct this divergence by adjusting mass height distribution, since the optimal values of
397 μ_{agg} and σ_{agg} can still be obtained from $\Delta_{downwind}^2$, and Δ_{area}^2 . As with the Crater peak (Spurr)
398 simulations, the isomass lines are jagged and patchy; an artifact of high relief. (The most distal
399 sample location lies at 4.3 km elevation on the west shoulder of Mount McKinley). Although
400 the value of μ_{agg} (2.4ϕ , 0.20mm) portrayed in Fig. 13 is close to optimal in Fig. 9j, many sample
401 points do not plot in Fig. 13b because modeled mass load is zero. And most values of Δ^2 are
402 high—0.99, largely because of the disparity in axis dispersal directions and the consequent fact
403 that sample points lie outside the modeled deposit. The reason that Δ^2 shows a clear minimum,
404 around $\mu_{agg}=2.4\phi$ (0.20mm) in Fig. 9j, is apparent from Figs. S131-S172 which show that, as
405 μ_{agg} decreases in size, the modeled deposit extends farther north and takes a clear turn to the
406 northeast, overlapping more with the mapped deposit. These figures also illuminate why
407 $\Delta_{downwind}^2$ is optimal at $\mu_{agg}=2.3$; because modeled and mapped loads come into best agreement
408 along the dispersal axis for aggregates of this size. Δ_{area}^2 is optimized at $\mu_{agg}<1$ because the
409 area of the 1 kg m^{-2} isomass diverges below the mapped value, and the area of the 0.01 kg m^{-2}
410 isomass diverges above observed, as aggregate size increases. The isomass lines are drawn
411 based on sparse data and are the least reliable of the datasets used in this comparison.

412 5 Discussion and Conclusions

413 The overall derived values of μ_{agg} have a narrow range between ~ 2.1 - 2.5ϕ (0.18-0.23mm),
414 despite large variations in erupted mass (0.25 - $50 \times Tg$), plume height (8.5-25 km), mass fraction



415 of fine (<0.063mm) ash (3-59%), atmospheric temperature, and water content between these
416 eruptions. The value of this narrow range depends strongly on other inputs, such as particle
417 density, shape factor, and Suzuki factor. But, holding those factors constant, the similarity in
418 this range between these four eruptions is noteworthy.

419 The overall agreement in modeled mean aggregate size (μ_{agg}) suggests that accelerated fine-
420 ash deposition may be treated as a discrete process, insensitive to eruptive style or magnitude.
421 It seems unlikely that these varied eruptions would produce aggregates of the same size, density,
422 and morphology. A combination of processes removed ash. Our approach captures these
423 processes implicitly, ignoring the microphysics.

424 What sort of processes could evolve in the cloud? Some possibilities are illustrated in Fig. A1.
425 The evolution starts with ejection of particles from that vent whose size ranges from microns
426 to meters. For an eruption having the TPSD of Mount St. Helens, the rising plume would have
427 contained 10^6 - 10^8 particles per cubic meter with diameter between 10-30 μm that collided with
428 larger particles hundreds of thousands of times per second. High collision rates and the
429 availability of liquid water in the plume would have led to rapid aggregation. Freezing of liquid
430 water and riming would have shifted the maximum possible size of aggregates towards mm to
431 cm sizes. Mud rain, observed falling at Mount St. Helens (Waitt, 1981) and ice aggregates
432 collected near the vent at Redoubt (Van Eaton et al., in press), are evidence of these processes.

433 In the downwind cloud particle concentrations were lower, turbulence was less intense, a
434 smaller range of particle sizes existed, and, for all four eruptions, atmospheric temperatures
435 near the plume top were well below freezing (Table 5), leading to presumably slow aggregation
436 rates. However, at least two other processes may help settle ash from downwind clouds. One
437 is gravitational overturn. Experiments (Carazzo and Jellinek, 2012) have observed that fine ash
438 settles toward the bottom of ash clouds as they expand and move downwind, accumulating
439 gravitationally unstable particle boundary layers that eventually overturn and cause the entire
440 air mass to settle rapidly. At Eyjafjallajökull in 2010, gravitational convective instabilities
441 formed within 10km of the vent, presumably as a result of accumulation of coarse ash over a
442 period of minutes (Manzella et al., 2015). The development of fine-ash particle boundary layers
443 presumably takes longer, perhaps hours, although the underlying processes remain a subject of
444 active research.



445 A second process is hydrometeor growth. In some cases, magmatic and (or) externally-derived
446 water in the eruption cloud may condense on ash particles and initiate hydrometeor growth.
447 Both hydrometeor growth and gravitational overturn have been suggested to produce the
448 mammatus clouds that developed in mid-day over central Washington on 18 May 1980 and
449 signaled mass settling (Durant, 2015; Durant et al., 2009; Carazzo and Jellinek, 2012).
450 Mammatus descent rates are typically meters per second (Schultz et al., 2006), much faster than
451 the settling rate of individual ash particles ($<0.1 \text{ m s}^{-1}$) or even of ash aggregates ($<\sim 1 \text{ m s}^{-1}$,
452 Fig. 5).

453 The extent to which these processes operated at Crater Peak, Ruapehu, and Redoubt is
454 unknown. Cloud structures were not observed during the nighttime eruptions of Redoubt and
455 Crater Peak (Spurr). And although virga-like structures can be seen in some near-vent photos
456 of Ruapehu (Bonadonna et al., 2005, Fig. 9a), we have seen no documentation of such
457 instabilities farther downwind.

458 For operational forecasting, these mechanisms cannot be considered in any case, because no
459 operational model has the capability to resolve these processes. The fact that these eruptions
460 can all be reasonably modeled using similar inputs for aggregate size is convenient, even if the
461 model does not calculate the processes involved. The agreement suggests that model forecasts
462 can still be useful during the coming years. Future work will focus on the development of more
463 sophisticated algorithms that account for cloud microphysics.

464 **6 Appendix**

465 The rate and extent of ash aggregation are sensitive to changes in both eruptive
466 conditions and background meteorology. Despite the complexity of the process, field studies
467 and laboratory experiments have highlighted key spatial and temporal controls. For example,
468 large aggregates, including frozen accretionary lapilli, tend to form near the volcanic source
469 and are particularly abundant in phreatomagmatic eruption deposits (Van Eaton et al., 2015;
470 Brown et al., 2012; Houghton et al., 2015). These are associated with precipitation-forming
471 processes occurring as particles collide in moist, turbulent updrafts rising above the volcanic
472 vent or ground-hugging density currents (Fig. A1). Field measurements indicate that near-
473 source aggregates commonly exceed 1 cm diameter (Wallace et al., 2013; Swanson et al., 2014;
474 Van Eaton and Wilson, 2013). In contrast, the low-density aggregates that produced the
475 Ritzville Bulge, 230 km downwind from Mount St. Helens, are thought to have been triggered
476 by mammatus cloud instabilities (Durant et al., (2009). As the cloud descended to warmer



477 atmospheric levels, the increasing proportion of liquid water increased the rate of aggregation
478 and fallout (red line, Fig. A1). These types of distal aggregates tend to be smaller than a
479 millimeter, forming in the downwind cloud up to hundreds of kilometers from source (Sorem,
480 1982; Dartayat, 1932).

481 Liquid water also influences aggregate morphology, density, and rate of formation. Laboratory
482 experiments have shown that wet ash (>10-15 wt.% liquid water) rapidly produces dense, sub-
483 spherical pellets, whereas drier conditions lead to low-density, electrostatically-bound clusters
484 (Schumacher and Schmincke, 1995; James et al., 2002; Van Eaton et al., 2012). Furthermore,
485 aggregation is a highly size-selective process – smaller particles (<0.25mm) have a much
486 greater likelihood of sticking (Gilbert and Lane, 1994; Schumacher and Schmincke, 1995; Van
487 Eaton et al., 2012). In this study, we do not attempt to address the detailed mechanisms of
488 aggregation, but consider the bulk impact on downwind deposits for practical applications in
489 ash dispersal forecasting.

490 **Author contributions**

491 L. Mastin conceived the study, did the model simulations and wrote most of the paper. A. Van
492 Eaton provided advice on aggregation processes and wrote the appendix. A. Durant provided
493 the data for Mount St. Helens and Crater Peak, and advice on aggregation processes that
494 occurred during those two eruptions.

495 **Acknowledgments**

496 We are grateful to the IAVCEI Commission on Tephra Hazard Modeling for posting data on
497 key eruptions that could be used for this study.

498 **References**

- 499 Armienti, P., Macedonio, G., and Pareschi, M. T.: A numerical model for simulation of tephra
 500 transport and deposition: Applications to May 18, 1980, Mount St. Helens eruption, *J.*
 501 *Geophys. Res.*, 93, 6463-6476, 1988.
- 502 Bonadonna, C., Macedonio, G., and Sparks, R. S. J.: Numerical modeling of tephra fallout
 503 associated with dome collapses and Vulcanian explosions: application to hazard
 504 assessment on Montserrat, in: the eruption of Soufriere Hills Volcano, Montserrat,
 505 edited by: Druitt, T. H., and Kokelaar, B. P., Geological Society of London memoirs,
 506 Geological Society of London, London, 517-537, 2002.
- 507 Bonadonna, C., and Houghton, B. F.: Total grain-size distribution and volume of tephra-fall
 508 deposits, *Bull. Volcanol.*, 67, 441-456, 2005.
- 509 Bonadonna, C., Phillips, J. C., and Houghton, B. F.: Modeling tephra sedimentation from a
 510 Ruapehu weak plume eruption, *J. Geophys. Res.*, 110, doi:10.1029/2004JB003515,
 511 2005.
- 512 Bonadonna, C., and Costa, A.: Estimating the volume of tephra deposits: A new simple
 513 strategy, *Geology*, 40, 415-418, 10.1130/g32769.1, 2012.
- 514 Briggs, G. A.: Plume rise and buoyancy effects, in: Atmospheric Science and Power
 515 Production, edited by: Randerson, D., U.S. Department of Energy, Washington, D.C.,
 516 327-366, 1984.
- 517 Brown, R. J., Bonadonna, C., and Durant, A. J.: A review of volcanic ash aggregation,
 518 *Physics and Chemistry of the Earth, Parts A/B/C*, 45-46, 65-78,
 519 <http://dx.doi.org/10.1016/j.pce.2011.11.001>, 2012.
- 520 Buurman, H., West, M. E., and Thompson, G.: The seismicity of the 2009 Redoubt eruption,
 521 *J. Volcanol. Geotherm. Res.*, 259, 16-30, 2013.
- 522 Carazzo, G., and Jellinek, A. M.: A new view of the dynamics, stability and longevity of
 523 volcanic clouds, *Earth Planet. Sci. Lett.*, 325-326, 39-51,
 524 <http://dx.doi.org/10.1016/j.epsl.2012.01.025>, 2012.
- 525 Carey, S., and Sigurdsson, H.: Influence of particle aggregation on deposition of distal tephra
 526 from the May 18, 1980, eruption of Mount St. Helens volcano, *J. Geophys. Res.*, 87,
 527 7061-7072, 1982.
- 528 Carey, S., Sigurdsson, H., Gardner, J. E., and Criswell, W.: Variations in column height and
 529 magma discharge during the May 18, 1980 eruption of Mount St. Helens, *J. Volcanol.*
 530 *Geotherm. Res.*, 43, 99-112, 1990.
- 531 Carey, S.: Modeling of tephra fallout from atmospheric eruptions, in: *Monitoring and*
 532 *Mitigation of Volcanic Hazards*, edited by: Scarpa, L. A., and Tilling, R. I., Springer
 533 Verlag, Berlin, 429-463, 1996.
- 534 Cornell, W., Carey, S., and Sigurdsson, H.: Computer simulation of transport and deposition
 535 of the campanian Y-5 ash, *J. Volcanol. Geotherm. Res.*, 17, 89-109, 1983.
- 536 Costa, A., Folch, A., and Macedonio, G.: A model for wet aggregation of ash particles in
 537 volcanic plumes and clouds: 1. Theoretical formulation, *J. Geophys. Res.*, 115,
 538 doi:10.1029/2009JB007175, 2010.
- 539 Dacre, H. F., Grant, A. L. M., Hogan, R. J., Belcher, S. E., Thomson, D. J., Devenish, B.,
 540 Marengo, F., Haywood, J., Ansmann, A., and Mattis, I.: The structure and magnitude
 541 of the ash plume during the initial phase of the Eyjafjallajökull eruption, evaluated
 542 using lidar observations and NAME simulations, *J. Geophys. Res.*, 116, D00U03,
 543 10.1029/2011JD015608, 2011.
- 544 Dartayot, M.: Observacion de la lluvia de cenizas del 11 de abril de 1932 en La Plata, *Revista*
 545 *astronómica.*, 4, 183-187, 1932.



- 546 Degruyter, W., and Bonadonna, C.: Improving on mass flow rate estimates of volcanic
547 eruptions, *Geophys. Res. Lett.*, 39, L16308, 10.1029/2012GL052566, 2012.
- 548 Devenish, B., Francis, P. N., Johnson, B. T., Sparks, R. S. J., and Thomson, D. J.: Sensitivity
549 analysis of dispersion modeling of volcanic ash from Eyjafjallajökull in May 2010, *J.*
550 *Geophys. Res.*, 117, doi:10.1029/2011JD016782, doi:10.1029/2011JD016782, 2012.
- 551 Durant, A., and Rose, W. I.: Sedimentological constraints on hydrometeor-enhanced particle
552 deposition: 1992 eruptions of Crater Peak, Alaska, *J. Volcanol. Geotherm. Res.*, 186,
553 40-59, 2009.
- 554 Durant, A. J., Rose, W. I., Sarna-Wojcicki, A. M., Carey, S., and Volentik, A. C.:
555 Hydrometeor-enhanced tephra sedimentation: Constraints from the 18 May 1980
556 eruption of Mount St. Helens (USA), *J. Geophys. Res.*, 114,
557 doi:10.1029/2008JB005756, 2009.
- 558 Durant, A. J.: RESEARCH FOCUS: Toward a realistic formulation of fine-ash lifetime in
559 volcanic clouds, *Geology*, 43, 271-272, 10.1130/focus032015.1, 2015.
- 560 Eichelberger, J. C., Keith, T. E. C., Miller, T. P., and Nye, C. J.: The 1992 eruptions of Crater
561 Peak vent, Mount Spurr Volcano, Alaska: Chronology and summary, in: *The 1992*
562 *Eruptions of Crater Peak Vent, Mount Spurr Volcano, Alaska. U.S. Geological*
563 *Survey Bulletin 2139*, edited by: Keith, T. E. C., U.S. Government Printing Office,
564 Washington, D.C., 1-18, 1995.
- 565 Eychenne, J., Cashman, K., Rust, A., and Durant, A.: Impact of the lateral blast on the spatial
566 pattern and grain size characteristics of the 18 May 1980 Mount St. Helens fallout
567 deposit, *Journal of Geophysical Research: Solid Earth*, 120, 6018-6038,
568 10.1002/2015JB012116, 2015.
- 569 Fierstein, J., and Nathenson, M.: Another look at the calculation of fallout tephra volumes,
570 *Bull. Volcanol.*, 54, 156-167, 1992.
- 571 Folch, A., Costa, A., Durant, A., and Macedonio, G.: A model for wet aggregation of ash
572 particles in volcanic plumes and clouds: 2. Model application, *J. Geophys. Res.*, 115,
573 B09202, 10.1029/2009jb007176, 2010.
- 574 Foxworthy, B. L., and Hill, M.: Volcanic eruptions of 1980 at Mount St. Helens: The first 100
575 days. USGS Prof. Paper 1249, U.S. Government Printing Office, Washington, D.C.,
576 1982.
- 577 Gardner, C. A., Cashman, K. V., and Neal, C. A.: Tephra-fall deposits from the 1992 eruption
578 of Crater Peak, Alaska: implications of clast textures for eruptive processes, *Bull.*
579 *Volcanol.*, 59, 537-555, 1998.
- 580 Genareau, K., Proussevitch, A. A., Durant, A. J., Mulukutla, G., and Sahagian, D. L.: Sizing
581 up the bubbles that produce very fine ash during explosive volcanic eruptions,
582 *Geophys. Res. Lett.*, 39, L15306, 10.1029/2012GL052471, 2012.
- 583 Gilbert, J. S., and Lane, S. J.: The origin of accretionary lapilli, *Bull. Volcanol.*, 56, 398-411,
584 1994.
- 585 Harris, D. M., Rose, W. I., Roe, R., and Thompson, M. R.: Radar observations of ash
586 eruptions, in: *The 1980 Eruptions of Mount St. Helens, Washington*, edited by:
587 Lipman, P. W., and Mullineaux, D. R., U.S. Government Printing Office, Washington,
588 D.C., 323-333, 1981.
- 589 Hewett, T. A., Fay, J. A., and Hoult, D. P.: Laboratory experiments of smokestack plumes in
590 a stable atmosphere, *Atmospheric Environment*, 5, 767-789, 1971.
- 591 Holasek, R. E., and Self, S.: GOES weather satellite observations and measurements of the
592 May 18, 1980, Mount St. Helens eruption, *J. Geophys. Res.*, 100, 8469-8487, 1995.
- 593 Houghton, B. F., White, J. D. L., and Van Eaton, A. R.: Phreatomagmatic and Related
594 Eruption Styles, in: *The Encyclopedia of Volcanoes*, edited by: Sigurdsson, H.,



- 595 Houghton, B. F., Rymer, H., Stix, J., and McNutt, S. R., Elsevier, Amsterdam, 537-
596 552, 2015.
- 597 Hoult, D. P., and Weil, J. C.: Turbulent plume in a laminar cross flow, *Atmospheric*
598 *Environment*, 6, 513-531, 1972.
- 599 Hurst, A. W., and Turner, J. S.: Performance of the program ASHFALL for forecasting
600 ashfall during the 1995 and 1996 eruptions of Ruapehu volcano, *New Zealand Journal*
601 *of Geology and Geophysics*, 42, 615-622, 1999.
- 602 James, M. R., Gilbert, J. S., and Lane, S. J.: Experimental investigation of volcanic particle
603 aggregation in the absence of a liquid phase, *J. Geophys. Res.*, 107,
604 doi:10.1029/2001JB000950, 2002.
- 605 Kalnay, E., Kanamitsu, M., Kistler, R., Collins, W., Deaven, D., Gandin, L., Iredell, M., Saha,
606 S., White, G., Woollen, J., Zhu, Y., Leetmaa, A., Reynolds, R., Chelliah, M.,
607 Ebisuzaki, W., Higgins, W., Janowiak, J., Mo, K. C., Ropelewski, C., Wang, J., Jenne,
608 R., and Joseph, D.: The NCEP/NCAR 40-Year Reanalysis Project, *Bulletin of the*
609 *American Meteorological Society*, 77, 437-471, 10.1175/1520-
610 0477(1996)077<0437:TNYRP>2.0.CO;2, 1996.
- 611 Klawonn, M., Frazer, L. N., Wolfe, C. J., Houghton, B. F., and Rosenberg, M. D.:
612 Constraining particle size-dependent plume sedimentation from the 17 June 1996
613 eruption of Ruapehu Volcano, New Zealand, using geophysical inversions, *Journal of*
614 *Geophysical Research: Solid Earth*, 119, 1749-1763, 10.1002/2013JB010387, 2014.
- 615 Liu, J., Salmond, J. A., Dirks, K. N., and Lindsay, J. M.: Validation of ash cloud modelling
616 with satellite retrievals: a case study of the 16–17 June 1996 Mount Ruapehu eruption,
617 *Natural Hazards*, 10.1007/s11069-015-1753-3, 2015.
- 618 Macedonio, G., Pareschi, M. T., and Santacroce, R.: A Numerical Simulation of the Plinian
619 Fall Phase of 79 A.D. Eruption of Vesuvius, *J. Geophys. Res.*, 93, 14817-14827, 1988.
- 620 Manzella, I., Bonadonna, C., Phillips, J. C., and Monnard, H.: The role of gravitational
621 instabilities in deposition of volcanic ash, *Geology*, 43, 211-214, 10.1130/g36252.1,
622 2015.
- 623 Mastin, L. G., Guffanti, M., Servranckx, R., Webley, P., Barsotti, S., Dean, K., Denlinger, R.,
624 Durant, A., Ewert, J. W., Neri, A., Rose, W. I., Schneider, D., Siebert, L., Stunder, B.,
625 Swanson, G., Tupper, A., Volentik, A., and Waythomas, C. F.: A multidisciplinary
626 effort to assign realistic source parameters to models of volcanic ash-cloud transport
627 and dispersion during eruptions, *J. Volcanol. Geotherm. Res.*, 186, 10-21, 2009.
- 628 Mastin, L. G., Randall, M., J., Schwaiger, H., and Denlinger, R.: User's Guide and Reference
629 to Ash3d: A Three-Dimensional Model for Atmospheric Tephra Transport and
630 Deposition, in: U.S. Geological Survey Open-File Report 2013-1122, 48, 2013a.
- 631 Mastin, L. G., Schwaiger, H., Schneider, D. J., Wallace, K. L., Schaefer, J., and Denlinger, R.
632 P.: Injection, transport, and deposition of tephra during event 5 at Redoubt Volcano,
633 23 March, 2009, *J. Volcanol. Geotherm. Res.*, 259, 201-213,
634 <http://dx.doi.org/10.1016/j.jvolgeores.2012.04.025>, 2013b.
- 635 Mastin, L. G.: Testing the accuracy of a 1-D volcanic plume model in estimating mass
636 eruption rate, *Journal of Geophysical Research: Atmospheres*, 119, 2013JD020604,
637 10.1002/2013JD020604, 2014.
- 638 McGimsey, R. G., Neal, C. A., and Riley, C.: Areal distribution, thickness, volume, and grain
639 size of tephra-fall deposits from the 1992 eruptions of Crater Peak vent, Mt. Spurr
640 volcano, Alaska, in: U.S. Geological Survey Open-File Report 01-0370, U.S.
641 Government Printing Office, Washington, D.C., 38, 2001.
- 642 Mesinger, F., DiMego, G., Kalnay, E., Mitchell, K., Shafran, P. C., Ebisuzaki, W., Jovic, D.,
643 Woollen, J., Rogers, E., Berbery, E. H., Ek, M. B., Fan, Y., Grumbine, R., Higgins,



- 644 W., Li, H., Lin, Y., Manikin, G., Parrish, D., and Shi, W.: North American Regional
 645 Reanalysis, *Bulletin of the American Meteorological Society*, 87, 343-360,
 646 DOI:10.1175/BAMS-87-3-343, 2006.
- 647 Nakagawa, M., Wada, K., Thordarson, T., Wood, C. P., and Gamble, J. A.: Petrologic
 648 investigations of the 1995 and 1996 eruptions of Ruapehu volcano, New Zealand:
 649 Formation of discrete and small magma pockets and their intermittent discharge, *Bull.*
 650 *Volcanol.*, 61, 15-31, 1999.
- 651 Neal, C. A., McGimsey, R. G., Gardner, C. A., Harbin, M., L., and Nye, C. J.: Tephra-fall
 652 deposits from the 1992 eruptions of Crater Peak, Mount Spurr, Alaska, in: *The 1992*
 653 *eruptions of Crater Peak, Mount Spurr, Alaska*, U.S.G.S. Bulletin 2139, edited by:
 654 Keith, T. E. C., U.S. Geological Survey, Washington, D.C., 65-79, 1995.
- 655 Prata, A. J., and Grant, I. F.: Retrieval of microphysical and morphological properties of
 656 volcanic ash plumes from satellite data: application to Mt. Ruapehu, New Zealand,
 657 *Quarterly Journal of the Royal Meteorological Society*, 127, 2153-2179, 2001.
- 658 Pyle, D. M.: The thickness, volume and grain size of tephra fall deposits, *Bull. Volcanol.*, 51,
 659 1-15, 1989.
- 660 Rice, C. J.: Satellite observations of the Mt. St. Helens eruption of 18 May 1980, in:
 661 *Technical Report, Aerosp. Corp., Space Sci. Lab., El Segundo, CA*, 1981.
- 662 Rose, W. I., Delene, D. J., Schneider, D. J., Bluth, G. J. S., Krueger, A. J., Sprod, I., McKee,
 663 C., Davies, H. L., and Ernst, G. G. J.: Ice in the 1994 Rabaul eruption cloud:
 664 implications for volcano hazard and atmospheric effects, *Nature*, 375, 477-479, 1995a.
- 665 Rose, W. I., Kostinski, A. B., and Kelley, L.: Real-time C-band radar observations of th 1992
 666 eruption clouds from Crater Peak, Mount Spurr Volcano, Alaska, in: *The 1992*
 667 *Eruptions of Crater Peak Vent, Mount Spurr Volcano, Alaska*. U.S. Geological
 668 Survey Bulletin 2139, edited by: Keith, T. E. C., U.S. Government Printing Office,
 669 Washington. D.C., 19-26, 1995b.
- 670 Rose, W. I., and Durant, A.: Fine ash content of explosive eruptions, *J. Volcanol. Geotherm.*
 671 *Res.*, 186, 32-39, 2009.
- 672 Rosenbaum, J., and Waitt, R.: A summary of eyewitness accounts of the May 18 eruption, in:
 673 *The 1980 eruptions of Mount St. Helens*, Washington, edited by: Lipman, P. W., and
 674 Mullineaux, D. R., U.S. Government Printing Office, Washington, D.C., 53-67, 1981.
- 675 Rutherford, M. J., Sigurdsson, H., Carey, S., and Davis, A.: The May 18, 1980, eruption of
 676 Mount St. Helens: 1, Melt composition and experimental phase equilibria, *J. Geophys.*
 677 *Res.*, 90, 2929-2947, 1985.
- 678 Sarna-Wojcicki, A. M., Shipley, S., Waitt, R., Dzurisin, D., and Wood, S. H.: Areal
 679 distribution, thickness, mass, volume, and grain size of air-fall ash from the six major
 680 eruptions of 1980, in: *The 1980 Eruptions of Mount St. Helens*, Washington; USGS
 681 Professional Paper 1250, edited by: Lipman, P. W., and Christiansen, R. L., U.S.
 682 Geological Survey, 577-601, 1981.
- 683 Schneider, D. J., and Hoblitt, R. P.: Doppler weather radar observations of the 2009 eruption
 684 of Redoubt Volcano, Alaska, *J. Volcanol. Geotherm. Res.*, 259, 133-144, 2013.
- 685 Schultz, D. M., Kanak, K. M., Straka, J. M., Trapp, R. J., Gordon, B. A., Zrnić, D. S., Bryan,
 686 G. H., Durant, A. J., Garrett, T. J., Klein, P. M., and Lilly, D. K.: The Mysteries of
 687 Mammatus Clouds: Observations and Formation Mechanisms, *Journal of the*
 688 *Atmospheric Sciences*, 63, 2409-2435, 10.1175/JAS3758.1, 2006.
- 689 Schumacher, R., and Schmincke, H. U.: Models for the origin of accretionary lapilli, *Bull.*
 690 *Volcanol.*, 56, 626-639, DOI: 10.1007/s004450050069 1995.



- 691 Schwaiger, H., Denlinger, R., and Mastin, L. G.: Ash3d: a finite-volume, conservative
692 numerical model for ash transport and tephra deposition, *J. Geophys. Res.*, 117,
693 doi:10.1029/2011JB008968, doi:10.1029/2011JB008968, 2012.
- 694 Scollo, S., Tarantola, S., Bonadonna, C., Coltelli, M., and Saltelli, A.: Sensitivity analysis and
695 uncertainty estimation for tephra dispersal models, *J. Geophys. Res.*, 113,
696 doi:10.1029/2006JB004864, doi:10.1029/2006JB004864, 2008.
- 697 Sisson, T. W.: Blast ashfall deposit of May 18, 1980 at Mount St. Helens, Washington, J.
698 *Volcanol. Geotherm. Res.*, 66, 203-216, 1995.
- 699 Sorem, R. K.: Volcanic ash clusters: Tephra rafts and scavengers, *J. Volcanol. Geotherm.*
700 *Res.*, 13, 63-71, 1982.
- 701 Sparks, R. S. J., Bursik, M. I., Carey, S. N., Gilbert, J. S., Glaze, L. S., Sigurdsson, H., and
702 Woods, A. W.: *Volcanic Plumes*, John Wiley & Sons, Chichester, 574 pp., 1997.
- 703 Suzuki, T.: A Theoretical model for dispersion of tephra, in: *Arc Volcanism: Physics and*
704 *Tectonics*, edited by: Shimozuru, D., and Yokoyama, I., Terra Scientific Publishing
705 Company, Tokyo, 95-113, 1983.
- 706 Swanson, D. A., Weaver, S. J., and Houghton, B. F.: Reconstructing the deadly eruptive
707 events of 1790 CE at Kīlauea Volcano, Hawai‘i, *Geological Society of America*
708 *Bulletin*, 10.1130/b31116.1, 2014.
- 709 Taddeucci, J., Scarlato, P., Montanaro, C., Cimarelli, C., Del Bello, E., Freda, C., Andronico,
710 D., Gudmundsson, M. T., and Dingwell, D. B.: Aggregation-dominated ash settling
711 from the Eyjafjallajökull volcanic cloud illuminated by field and laboratory high-speed
712 imaging, *Geology*, 39, 891-894, 10.1130/g32016.1, 2011.
- 713 Van Eaton, A. R., Muirhead, J. D., Wilson, C. J. N., and Cimarelli, C.: Growth of volcanic
714 ash aggregates in the presence of liquid water and ice: an experimental approach, *Bull.*
715 *Volcanol.*, 74, 1963-1984, 10.1007/s00445-012-0634-9, 2012.
- 716 Van Eaton, A. R., and Wilson, C. J. N.: The nature, origins and distribution of ash aggregates
717 in a large-scale wet eruption deposit: Oruanui, New Zealand, *J. Volcanol. Geotherm.*
718 *Res.*, 250, 129-154, 2013.
- 719 Van Eaton, A. R., Mastin, L. G., Herzog, M., Schwaiger, H. F., Schneider, D. J., Wallace, K.
720 L., and Clarke, A. B.: Hail formation triggers rapid ash aggregation in volcanic
721 plumes, *Nat Commun*, 6, 10.1038/ncomms8860, 2015.
- 722 Van Eaton, A. R., Mastin, L. G., Herzog, M., Schwaiger, H., Schneider, D., Wallace, D. A.,
723 and Clarke, A.: Hail formation as a mechanism of rapid ash aggregation in volcanic
724 clouds, *Nature Communications*, in press.
- 725 Waitt, R.: Devastating pyroclastic density flow and attendant air fall of May 18 - Stratigraphy
726 and sedimentology of deposits, in: *The 1980 Eruptions of Mount St. Helens*,
727 Washington. U.S. Geological Survey Professional Paper 1250, edited by: Lipman, P.
728 W., and Mullineaux, D. R., U.S. Government Printing Office, Washington, D.C., 438-
729 458, 1981.
- 730 Waitt, R., and Dzurisin, D.: proximal air-fall deposits from the May 18 eruption--stratigraphy
731 and field sedimentology, in: *The 1980 Eruptions of Mount St. Helens*, Washington,
732 edited by: Lipman, P. W., and Mullineaux, D. R., U.S. Geological Survey Professional
733 Paper 1250, U.S. Government Printing Office, Washington, D.C., 601-615, 1981.
- 734 Wallace, K. L., Schaefer, J. R., and Coombs, M. L.: Character, mass, distribution, and origin
735 of tephra-fall deposits from the 2009 eruption of Redoubt Volcano, Alaska—
736 Highlighting the significance of particle aggregation, *J. Volcanol. Geotherm. Res.*,
737 259, 145-169, <http://dx.doi.org/10.1016/j.jvolgeores.2012.09.015>, 2013.
- 738 Wilson, L., and Huang, T. C.: The influence of shape on the atmospheric settling velocity of
739 volcanic ash particles, *Earth Planet. Sci. Lett.*, 44, 311-324, 1979.



740 Woodhouse, M. J., Hogg, A. J., Phillips, J. C., and Sparks, R. S. J.: Interaction between
741 volcanic plumes and wind during the 2010 Eyjafjallajökull eruption, Iceland, Journal
742 of Geophysical Research: Solid Earth, 118, 92-109, 10.1029/2012JB009592, 2013.
743



744 **Tables**

745 Table 1: Input parameters for simulations. Vent elevation is given in kilometers above mean
 746 sea level.

| PARAMETER(S) | MOUNT ST. HELENS | SPURR | RUAPEHU | REDOUBT |
|---|-------------------------------------|---|--|-------------------------------------|
| MODEL DOMAIN | 42-49°N 124-110°W 0-35 km asl | 59-64°N 155.6- 141.4°W 0-17 km asl | 39.5-37.5°S 175-177°E 0-12km asl | 60-64°N 155-145°W 0-20km asl |
| VENT LOCATION | 122.18°W 46.2°N | 152.25°W 61.23°N | 175.56°E 39.28°S | 152.75°W 60.48°N |
| VENT ELEVATION (KM) | 2.00 | 2.30 | 2.80 | 2.30 |
| NODAL SPACING | 0.1° horizontal 1.0 km vertical | 0.1° horizontal 1.0 km vertical | 0.025° horizontal 0.5 km vertical | 0.07° horizontal 1.0 km vertical |
| ERUPTION START DATE (UTC) (YYYY.MM.DD) | 1980.05.18 | 1992.09.17 | 1996.06.16 1996.06.17 | 2009.03.23 |
| START TIME (UTC) | 1530 | 0803 UTC | 2030 UTC 0200 UTC | 1230 UTC |
| PLUME HEIGHT, KM ASL | See Table 2 | 13 | 8.5 | 15 |
| DURATION, HRS | See Table 2 | 3.6 | 4.5 2.0 | 0.33 |
| ERUPTED VOLUME KM ³ DRE | 0.2 (total) | 0.014 | 0.000643 0.000357 | 0.0017 |
| DIFFUSION COEFFICIENT <i>D</i> | 0 | 0 | 0 | 0 |
| SUZUKI CONSTANT <i>K</i> | 8 | 8 | 8 | 8 |
| PARTICLE SHAPE FACTOR <i>F</i> | 0.44 | 0.44 | 0.44 | 0.44 |
| AGGREGATE SHAPE FACTOR <i>F</i> | 1.0 | 1.0 | 1.0 | 1.0 |

747

748



749 Table 2: Time series of plume height and total erupted volume used in model simulations of
750 the Mount St. Helens ash cloud. H =plume height in km above sea level (a.s.l.), V =erupted
751 volume in million cubic meters dense-rock equivalent (DRE). The time series of plume height
752 approximates that measured by radar (Harris et al., 1981). We calculated a preliminary eruptive
753 volume for each eruptive pulse using the duration and the empirical relationship between plume
754 height and eruption rate (Mastin et al., 2009). This method underestimated the eruptive volume,
755 as noted in previous studies (Carey et al., 1990). Hence we adjusted the volume of each pulse
756 proportionately so that their total equals the 0.2 km^3 DRE estimated by Sarna-Wojcicki et al.
757 (1981). For the last two eruptive pulses, start times in UTC, marked with asterisks, are on 19
758 May in UTC time. All other start times are on 18 May.

Plume height (H), duration (D) and volume (V)

| start | | D | H | V |
|-------|-------|-----|--------|---------------------------------------|
| PDT | UTC | min | km asl | $\times 10^6 \text{ m}^3 \text{ DRE}$ |
| 8:30 | 1530 | 30 | 25 | 3.247 |
| 9:00 | 1600 | 36 | 15.3 | 0.077 |
| 9:36 | 1636 | 54 | 13.7 | 0.356 |
| 10:30 | 1730 | 45 | 15.3 | 0.502 |
| 11:15 | 1815 | 30 | 16.1 | 0.426 |
| 11:45 | 1845 | 42 | 17.4 | 0.615 |
| 12:27 | 1927 | 48 | 17.4 | 0.615 |
| 13:15 | 2015 | 60 | 14.6 | 0.183 |
| 14:15 | 2115 | 45 | 14.7 | 0.535 |
| 15:30 | 2230 | 60 | 15.8 | 0.691 |
| 16:30 | 2330 | 60 | 19.2 | 0.700 |
| 17:30 | 0030* | 60 | 7.7 | 1.945 |
| 18:30 | 0130* | 60 | 6.2 | 0.020 |

759



760 Table 3. Statistical measures of fit used in this paper

| Name | Formula | Explanation |
|---------------------------------|--|---|
| Point-by-point method | $\Delta^2 = \left[\frac{\sum_{i=1}^N (m_{m,i} - m_{o,i})^2}{\sum_{i=1}^N m_{o,i}^2} \right]^{1/2}$ | The mass load $m_{o,i}$ observed at each sample location i is compared with modeled mass load $m_{m,i}$ at the same location. Squared differences are summed to the total number of sample points N , and normalized to the sum of squares of the observed mass loads. |
| Downwind thinning method | $\Delta_{downwind}^2 = \frac{1}{M} \sum_{j=1}^M (\log(m_{m,j} / m_{o,j}))^2$ | The log of modeled mass load $m_{m,j}$ at a point j on the dispersal axis, is compared with the observation-based value $m_{o,j}$ expected at that location based on a trend line drawn between field measurements along the axis (Fig. 7). Differences between $m_{m,j}$ and $m_{o,j}$ are calculated on a log scale, squared, and summed. |
| Isomass area method | $\Delta_{area}^2 = \left[\frac{\sum_{i=1}^L (A_{m,i} - A_{o,i})^2}{\sum_{i=1}^L A_{o,i}^2} \right]^{1/2}$ | This method calculates the area $A_{m,i}$ of the modeled deposit that exceeds a given mass load i by summing the area of all model nodes that meet this criterion. It then takes the difference between $A_{m,i}$ and the area $A_{o,i}$ within same isomass line mapped from field observations. The sum of the squares of these differences, normalized to the sum of the squared mapped isopach areas, gives the index Δ_{area}^2 . |

761
 762
 763



764 Table 4: percentage of fine ash assigned to different size bins for different values of σ_{agg} .

| | $\mu_{agg} - 0.2$ | $\mu_{agg} - 0.1$ | μ_{agg} | $\mu_{agg} + 0.1$ | $\mu_{agg} + 0.2$ |
|----------------------|-------------------|-------------------|-------------|-------------------|-------------------|
| $\sigma_{agg} = 0.1$ | | | 100% | | |
| $\sigma_{agg} = 0.2$ | | 25% | 50% | 25% | |
| $\sigma_{agg} = 0.3$ | 10% | 20% | 40% | 20% | 10% |

765

766



767 Table 5: Atmospheric temperature profiles during the eruptions at Mount St. Helens, Crater
 768 Peak (Spurr), Ruapehu, and Redoubt volcanoes. Profile for Mount St. Helens is for 18 May
 769 1980, 1800 UTC, interpolated to the location of Ritzville, Washington (47.12°N, 118.38°W).
 770 For Crater Peak (Spurr) the profile is for 17 September 1992, 1200 UTC, interpolated to the
 771 location of Palmer, Alaska (61.6°N, 149.11°W). For Ruapehu the temperature profile is for
 772 17 June 1996, 0000 UTC, interpolated to the location of Ruapehu. For Redoubt the sounding
 773 was for 23 March 2009, 1200 UTC, at 62°N, 153°W. All soundings were taken from using
 774 RE1 reanalysis data at <http://ready.arl.noaa.gov/READYamet.php>. For Mount St. Helens,
 775 the freezing elevation was also checked using data from the North American Regional
 776 Reanalysis (NARR) model (Mesinger et al., 2006), available at the same NOAA site, and
 777 found to be 3.3 km, similar to that given below by the RE1 model.
 778

| p (hPa) | <i>Mount St. Helens</i> | | <i>Crater Peak (Spurr)</i> | | <i>Ruapehu</i> | | <i>Redoubt</i> | |
|---------|-------------------------|-------|----------------------------|-------|----------------|-------|----------------|-------|
| | z (m) | T (C) | z (m) | T (C) | z (m) | T (C) | z (m) | T (C) |
| 10 | 31,381 | -39.9 | 31,137 | -41.8 | 30,632 | -54.9 | 30,179 | -61.9 |
| 20 | 26,713 | -47.5 | 26,535 | -51.0 | 26,239 | -57.9 | 25,891 | -62.1 |
| 30 | 24,067 | -52.1 | 23,920 | -54.4 | 23,673 | -56.6 | 23,385 | -61.3 |
| 50 | 20,786 | -55.7 | 20,660 | -55.5 | 20,441 | -57.1 | 20,185 | -57.6 |
| 70 | 18,646 | -55.8 | 18,515 | -55.6 | 18,307 | -56.4 | 18,049 | -55.1 |
| 100 | 16,377 | -55.4 | 16,241 | -55.3 | 16,041 | -56 | 15,759 | -53.1 |
| 150 | 13,782 | -55.1 | 13,646 | -56.0 | 13,439 | -54.2 | 13,133 | -51 |
| 200 | 11,962 | -58.3 | 11,833 | -58.9 | 11,613 | -58.6 | 11,255 | -50.4 |
| 250 | 10,552 | -53.4 | 10,412 | -51.3 | 10,214 | -58.3 | 9,814 | -54.7 |
| 300 | 9,355 | -44 | 9,200 | -41.0 | 9,057 | -53.4 | 8,652 | -55.5 |
| 400 | 7,355 | -28.5 | 7,174 | -25.0 | 7,151 | -38.9 | 6,764 | -41.9 |
| 500 | 5,716 | -16.4 | 5,519 | -15.5 | 5,576 | -26.7 | 5,225 | -33.9 |
| 600 | 4,318 | -6.9 | 4,126 | -10.2 | 4,231 | -15.5 | 3,929 | -27.4 |
| 700 | 3,100 | 0.1 | 2,929 | -6.7 | 3,049 | -8.6 | 2,802 | -19.5 |
| 850 | 1,515 | 10.3 | 1,397 | -2.0 | 1,524 | -1.4 | 1,330 | -9.7 |
| 925 | -- | -- | 722 | -0.2 | 844 | 3.8 | 675 | -8.9 |

779

780



781 **Figure captions**

782 Figure 1: Maps of the deposits investigated in this work: (a) Mount St. Helens, 18 May 1980;
783 (b) Crater Peak, 16-17 September, 1992; (c) Ruapehu, 17 June, 1996; and (d) Redoubt, 23
784 March, 2009. Isomass lines for Mount St. Helens were digitized from Fig. 338 in Sarna-
785 Wojcicki et al. (1981); for Crater Peak from Fig. 15 in McGimsey et al. (2001); for Ruapehu
786 from Fig. 1 of Bonadonna and Houghton (2005); and for Redoubt from Wallace et al. (2013).
787 Isomass values are all in kg m^{-2} . Colored markers represent locations where isomass was
788 sampled, with colors corresponding to the mass load shown in the color table. Black dashed
789 lines indicate the dispersal axis. Sample locations for Mount St. Helens taken from
790 supplementary material in Durant et al. (2009); for Redoubt from Wallace et al. (2013), for
791 Crater Peak from McGimsey et al. (2001) and for Ruapehu, from data posted online at the
792 IAVCEI Commission on Tephra Hazard Modeling database (<http://dbstr.ct.ingv.it/iavcei/>
793 (Bonadonna and Houghton, 2005; Bonadonna et al., 2005)).

794 Figure 2: Total particle size distribution for each of the deposits studied: (a) Mount St. Helens,
795 (b) Crater Peak (Mount Spurr), (c) Ruapehu, and (d) Redoubt. Gray bars show the original
796 TPSD before aggregation. Black bars show the sizes not involved in aggregation; red bars show
797 sizes of aggregate classes used in Figs. 10-13.

798 Figure 3: Mass load versus downwind distance along the dispersal axis for the deposits of (a)
799 Mount St. Helens, (b) Crater Peak (Mount Spurr), (c) Ruapehu, and (d) Redoubt. Squares
800 indicate sample points within 20 km of the dispersal axis, with the grayscale value indicating
801 the distance from the dispersal axis following the colorbar in (a). The dash trend lines represent
802 interpolated values of the mass load that are compared with modeled values to calculate
803 $\Delta_{downwind}^2$.

804 Figure 4: Log mass load versus the square root of the area within isomass lines mapped for the
805 (a) Mount St. Helens; (b) Crater Peak (Spurr); (c) Ruapehu; and (d) Redoubt deposits. Also
806 shown are best-fit lines, drawn by visual inspection, using either one line segment (Ruapehu,
807 Redoubt) or two, where justified (Spurr, St. Helens). Triangular markers are marked with labels
808 indicating the approximate percentage of the deposit mass lying inboard of these points, as
809 calculated using equations derived from Fierstein and Nathenson (1992).

810 Figure 5: (a) Transport distance versus average fall velocity, assuming a 15.1 m s^{-1} wind speed,
811 equal to the average wind speed at Mount St. Helens between 0 and 15 km, and a fall distance



812 of 15 km. The vertical shaded bar represents the distance of Ritzville. Labels on dots give the
813 average diameter of a round aggregate having a density of 600 kg m^{-3} and the given fall velocity.
814 (b) Average fall velocity between 0 and 15 km elevation, versus aggregate diameter, for round
815 aggregates having densities ranging from 200 to $2,500 \text{ kg m}^{-3}$. The horizontal shaded bar
816 represents the range of average fall velocities that would land in Ritzville. Fall velocities are
817 calculated using relations of Wilson and Huang (1979).

818 Figure 6: Deposit maps for simulations using a single size class representing an aggregate with
819 ϕ size 1.9 and density 600 kg m^{-3} , using three shape factors: (a) $F=0.44$; (b) $F=0.7$; and (c)
820 $F=1.0$. Inset figures illustrate ellipsoids having the given shape factor, assuming $b=(a+c)/2$.

821 Figure 7: Deposit map for simulations using a single size class representing an aggregate with
822 $F=1.0$, ϕ size 2.4ϕ and density 600 kg m^{-3} . Figs. 7a, b, and c, illustrate the deposit distribution
823 using Suzuki k values of 4, 8, and 12, while Fig. 7d illustrates the deposit distribution resulting
824 from release of all the erupted mass from a single node at the top of the plume. Inset plots
825 schematically illustrate the vertical distribution of mass with height in the plume for each of
826 these cases. Simulations used other input values as given in Table 1. Colored dots represent
827 sample locations with colors indicating the sampled mass load, as in Fig. 1a.

828 Figure 8: Results of Mount St. Helens simulations using a single size class of round aggregates
829 in each simulation: $\phi=1.8, 2.0, 2.2, 2.4$, and 2.6 in (a), (b), (c), (d), and (e); (f) shows the mapped
830 mass load, digitized from Fig. 338 in Sarna-Wojcicki et al. [1981]. Markers in each figure
831 provide the sample locations, with colors indicating the mass load measured at each location,
832 as shown in the color bar. Lines are contours of mass load with colors giving their values. The
833 mass load values of the contour lines, from lowest to highest, are 0.01, 0.1, 0.5, 1, 5, 10, 20, 30,
834 50, 80, and 100 kg m^{-2} respectively.

835 Figure 9: Contours of Δ^2 (left column), $\Delta_{downwind}^2$ (middle column), and Δ_{area}^2 (right column) as
836 a function of σ_{agg} and μ_{agg} for deposits from Mount St. Helens (top row); Crater Peak (Mount
837 Spurr, second row); Ruapehu (third row), and Redoubt (bottom row). The values of these
838 contour lines are indicated by the color using the color bar at the right. Maximum and minimum
839 values in the color scale are given within each frame. The best agreement between model and
840 mapped data is indicated by the deep blue and purple contours; the worst is indicated by the
841 yellow contours. Regions of each plot where agreement is best is indicated by the word "Lo".



842 Figure 10: Results of the Mount St. Helens simulation that provides approximately the best fit
843 to mapped data ($\mu_{agg}=2.4\phi$ and $\sigma_{agg}=0.3\phi$). (a) Deposit map with modeled isomass lines and
844 dots that represent field measurements with colors indicating the field values of the mass load,
845 corresponding to the color bar at left. The black dashed line indicates the dispersal axis of the
846 mapped deposit whereas the solid black line with dots indicates the dispersal axis of the
847 modeled deposit (the latter lies mostly on top of the former and obscures it). (b) Log of modeled
848 mass load versus measured mass load at sample locations. Black dashed line is the 1:1 line;
849 dotted lines above and below indicate modeled values 10 and 0.1 times that measured. Gray
850 dots lay outside the range of downwind distances covered by trend lines in Fig. 6 and therefore
851 were not included in the calculation of Δ^2 . (c) Log of measured mass load (black and gray dots),
852 and modeled mass load (black line with dots) versus distance downwind along the dispersal
853 axis. The black dashed line is the same trend line as in Fig. 7a. Gray dots were not included in
854 the calculation of Δ_{area}^2 . (d) Log of mass load versus square root of area contained within
855 isomass lines. Black squares are from the mapped deposit, red squares from the modeled one.

856 Figure 11: Results of the Crater Peak (Mount Spurr) simulation that provides approximately the
857 best fit to mapped data ($\mu_{agg}=1.8\phi$ and $\sigma_{agg}=0.3\phi$). The features in the sub-figures are as
858 described in Fig. 10. “CP” in Fig. 11a refers to the Crater Peak vent.

859 Figure 12: Results of the Ruapehu simulation that provides approximately the best fit to mapped
860 data ($\mu_{agg}=2.4\phi$ and $\sigma_{agg}=0.3\phi$). The features in the sub-figures are as described in Fig. 10.

861 Figure 13: Results of the Redoubt simulation that provides a reasonable fit to mapped data (
862 $\mu_{agg}=2.4\phi$ and $\sigma_{agg}=0.3\phi$). The features in the sub-figures are as described in Fig. 10.

863 Figure 14: Modeled mass load of the Mount St. Helens eruption for four cases using μ_{agg}
864 $=2.4\phi$, $\sigma_{agg}=0.3\phi$, and different diffusion coefficients: (a) $D=0\text{ m}^2\text{ s}^{-1}$, (b) $3\times 10^2\text{ m}^2\text{ s}^{-1}$, (c)
865 $1\times 10^3\text{ m}^2\text{ s}^{-1}$, and (d) $3\times 10^3\text{ m}^2\text{ s}^{-1}$. Other inputs are as given in Tables 1 and 2. Lines are
866 isomass contours of modeled mass load and colored dots are sample locations. Colors of the
867 dots and lines give the mass load corresponding to the color table.

868 Figure 15: Modeled mass load of the Ruapehu eruption for four cases using $\mu_{agg}=2.4\phi$, σ_{agg}
869 $=0.3\phi$, and different diffusion coefficients: (a) $D=0\text{ m}^2\text{ s}^{-1}$, (b) $1\times 10^2\text{ m}^2\text{ s}^{-1}$, (c) $3\times 10^2\text{ m}^2\text{ s}^{-1}$,



870 and (d) $1 \times 10^3 \text{ m}^2 \text{ s}^{-1}$. Other inputs are as given in Table 1. Lines are isomass contours of
871 modeled mass load and colored dots are sample locations. Colors of the dots and lines give the
872 mass load corresponding to the color table.

873 Figure A1: Illustration of the path taken by coarse aggregates that fallout in proximal sections,
874 less than a few plume heights from the source (left), and fine aggregates that fall out in distal
875 sections (right). Among distal fine aggregates, we show the path taken by those that might have
876 formed within or below the downwind cloud as hypothesized by Durant et al. (2009) (red
877 dashed line), and those that were transported downwind without changing size, as calculated
878 by Ash3d (blue dashed line). Also illustrated are some key processes that might influence the
879 distribution of fine, distal ash, including development of gravitational instability and overturn
880 within the downwind cloud (Carazzo and Jellinek, 2012), and the development of
881 hydrometeors as descending ash approaches the freezing elevation (Durant et al., 2009).

882 Figures S001-S004: Figures analogous to Figs. 10, 11, 12, and 13, respectively, but with no
883 particle aggregation.

884 Figures S005-S046: Figures analogous to Fig. 10, but for different values of μ_{agg} and σ_{agg}
885 given in their labels.

886 Figures S047-S088: Figures analogous to Fig. 11, but for different values of μ_{agg} and σ_{agg}
887 given in their labels.

888 Figures S089-S130: Figures analogous to Fig. 12, but for different values of μ_{agg} and σ_{agg}
889 given in their labels.

890 Figures S131-S172: Figures analogous to Fig. 13, but for different values of μ_{agg} and σ_{agg}
891 given in their labels.

892 Figure S173: Figure analogous to Fig. 12, but using

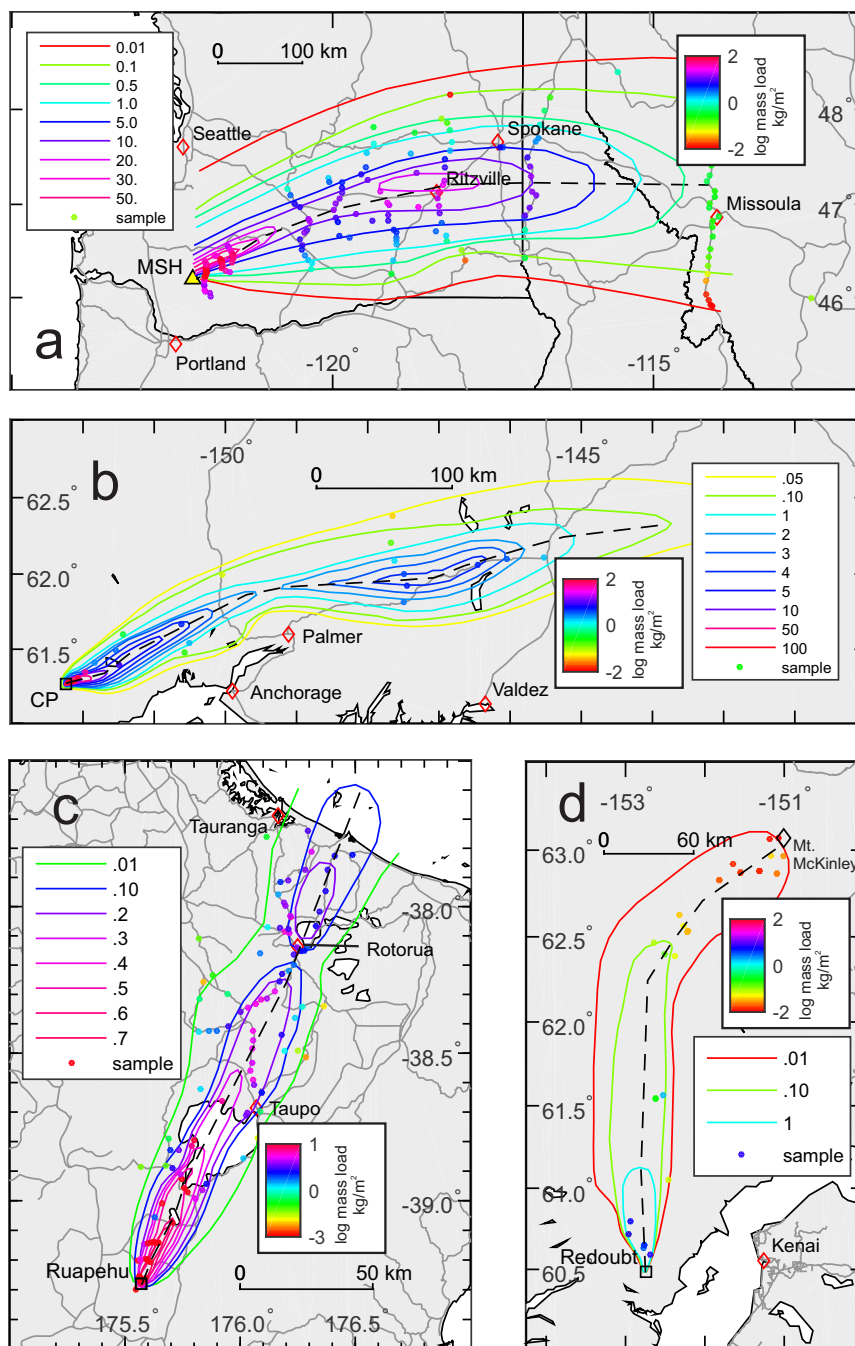


Figure 1

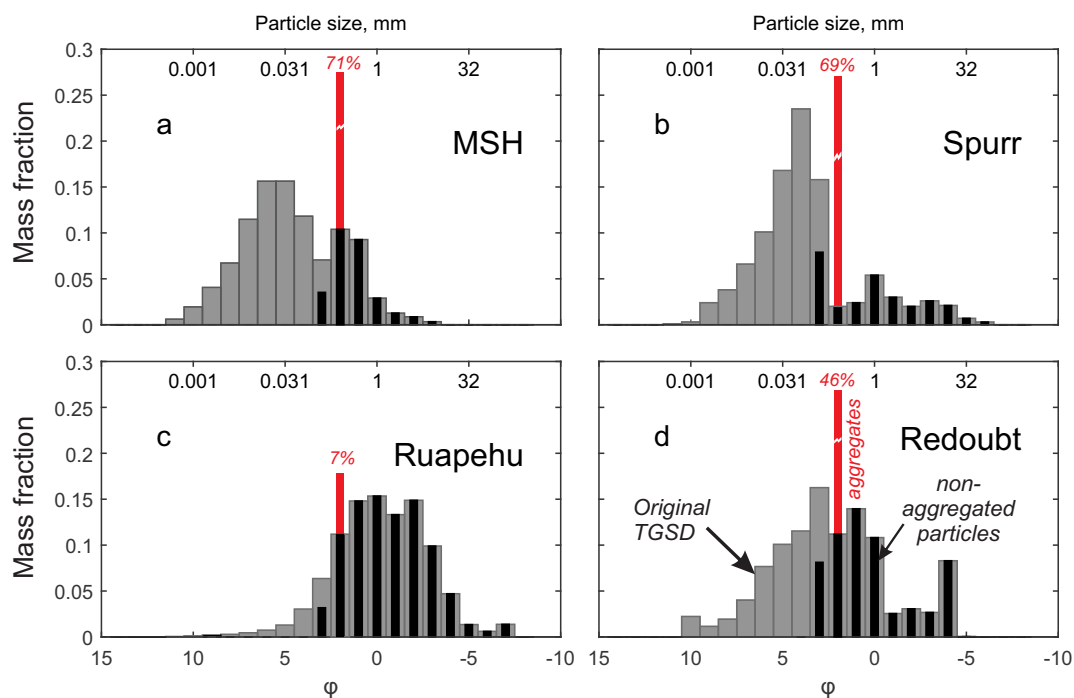


Figure 2

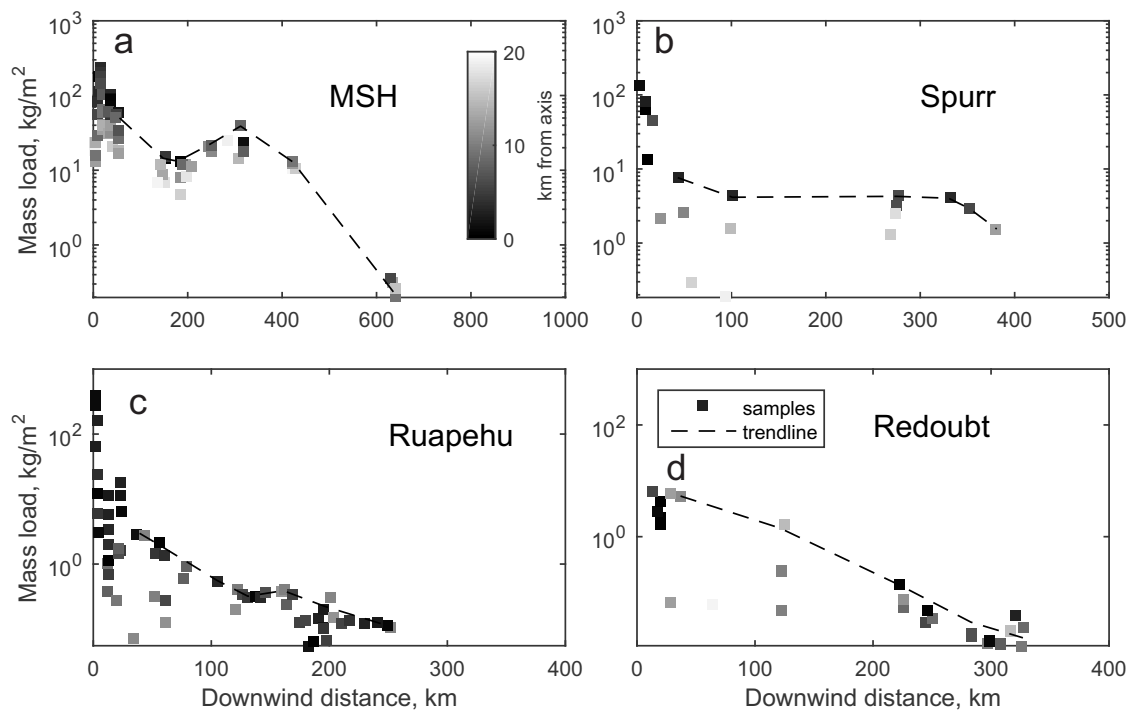


Figure 3

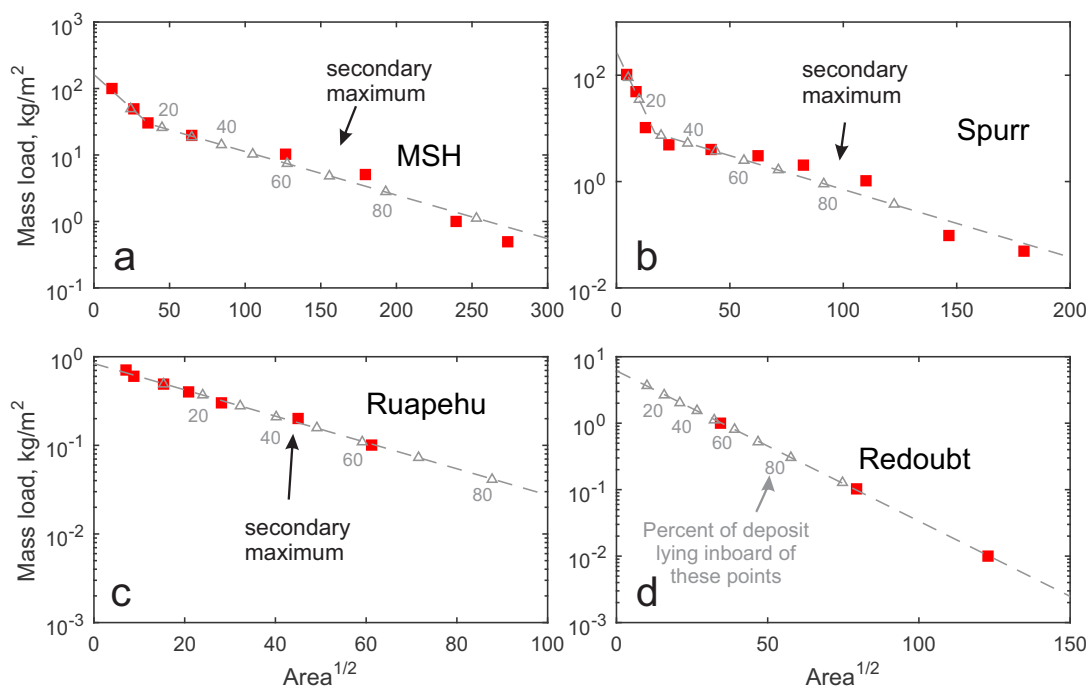


Figure 4

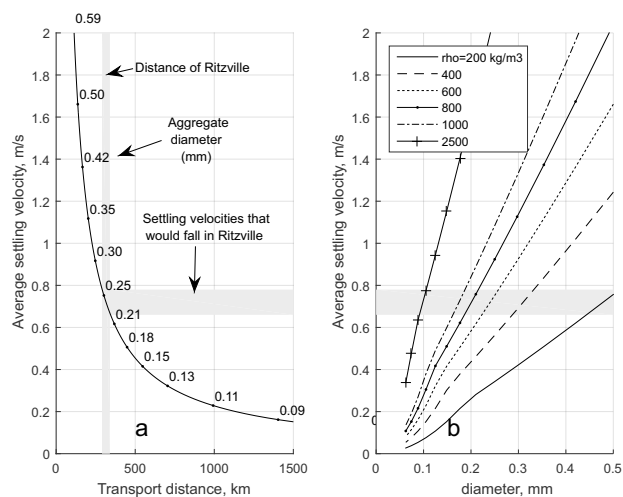


Figure 5

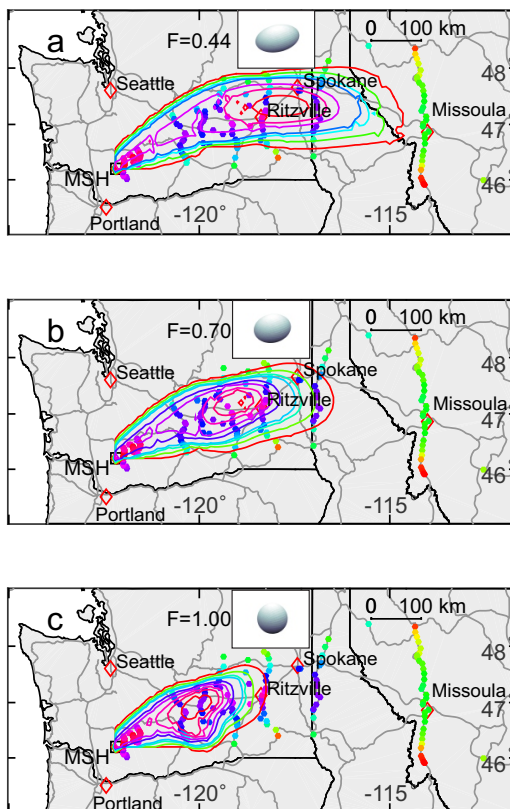


Figure 6

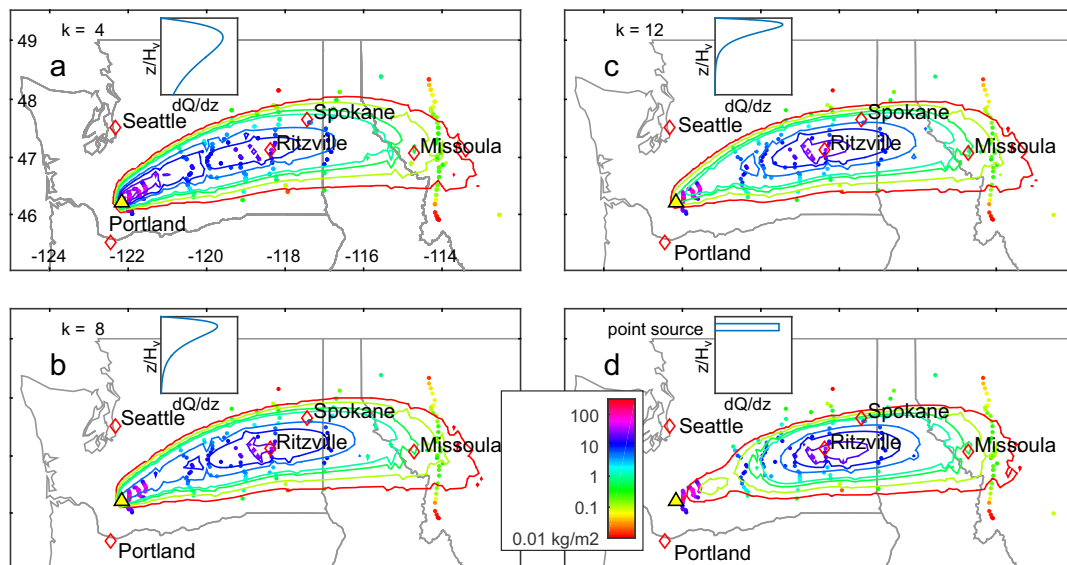


Figure 7

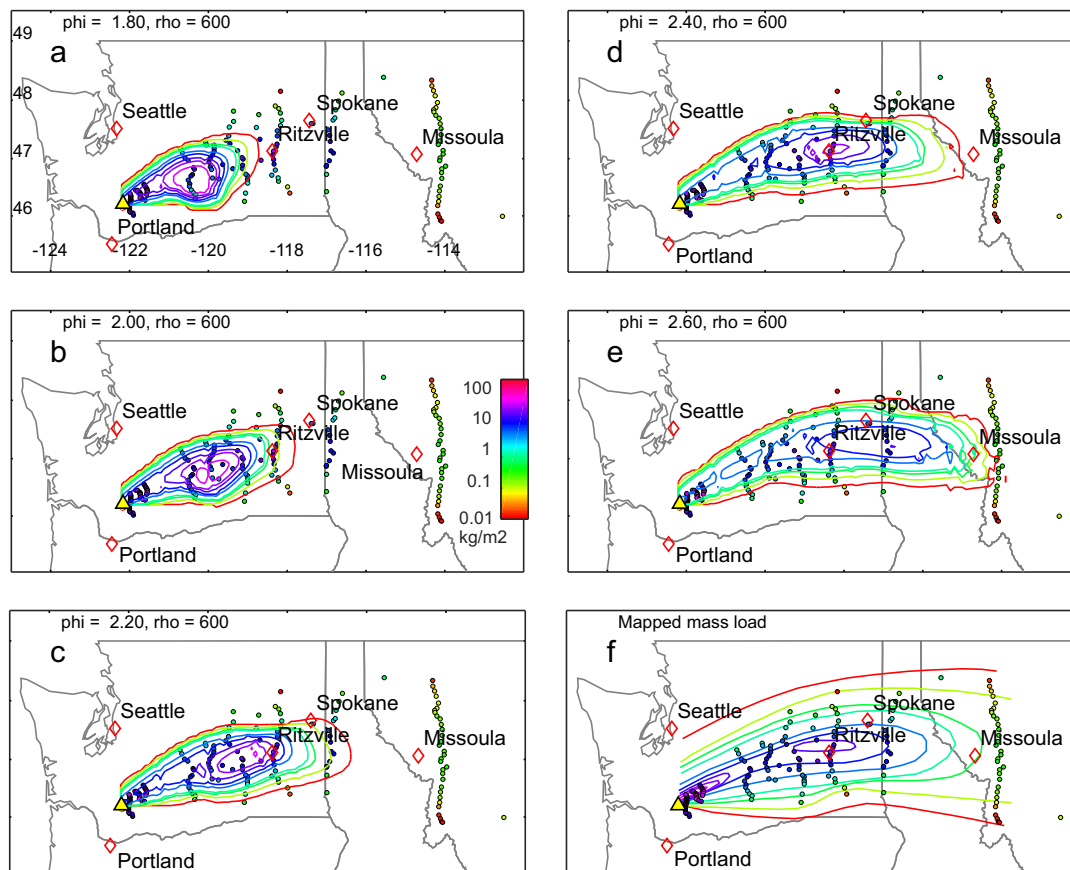


Figure 8

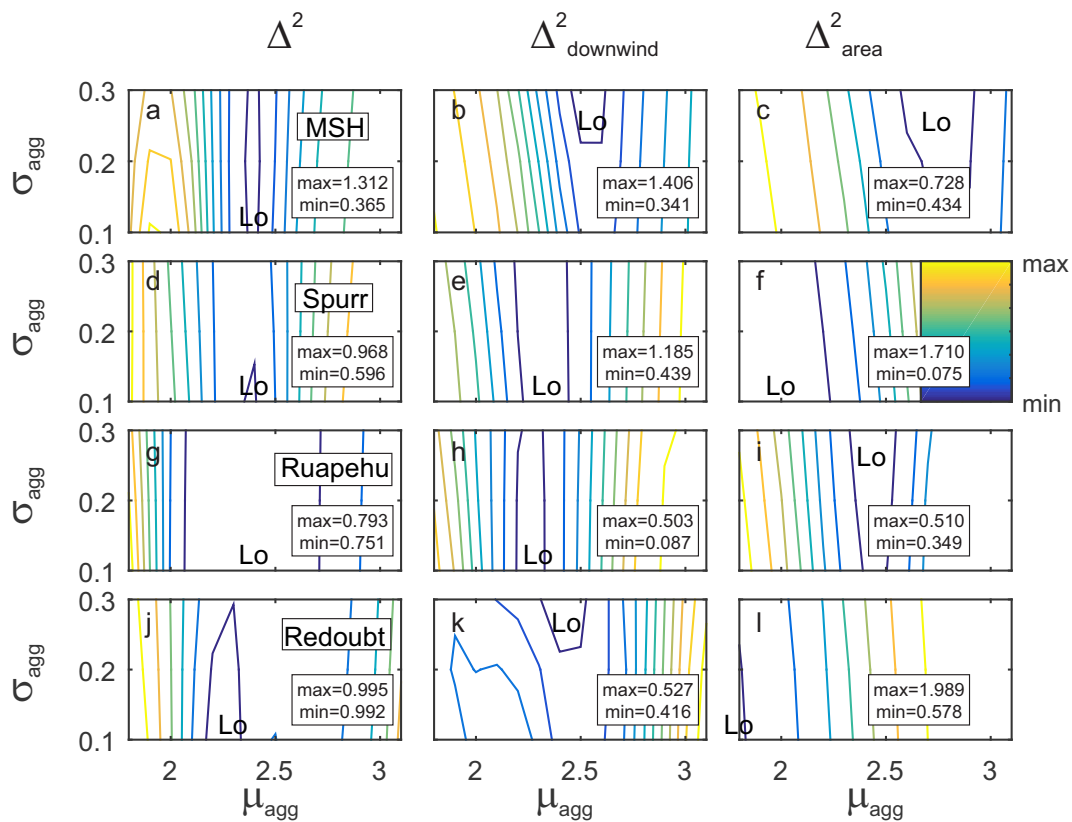


Figure 9

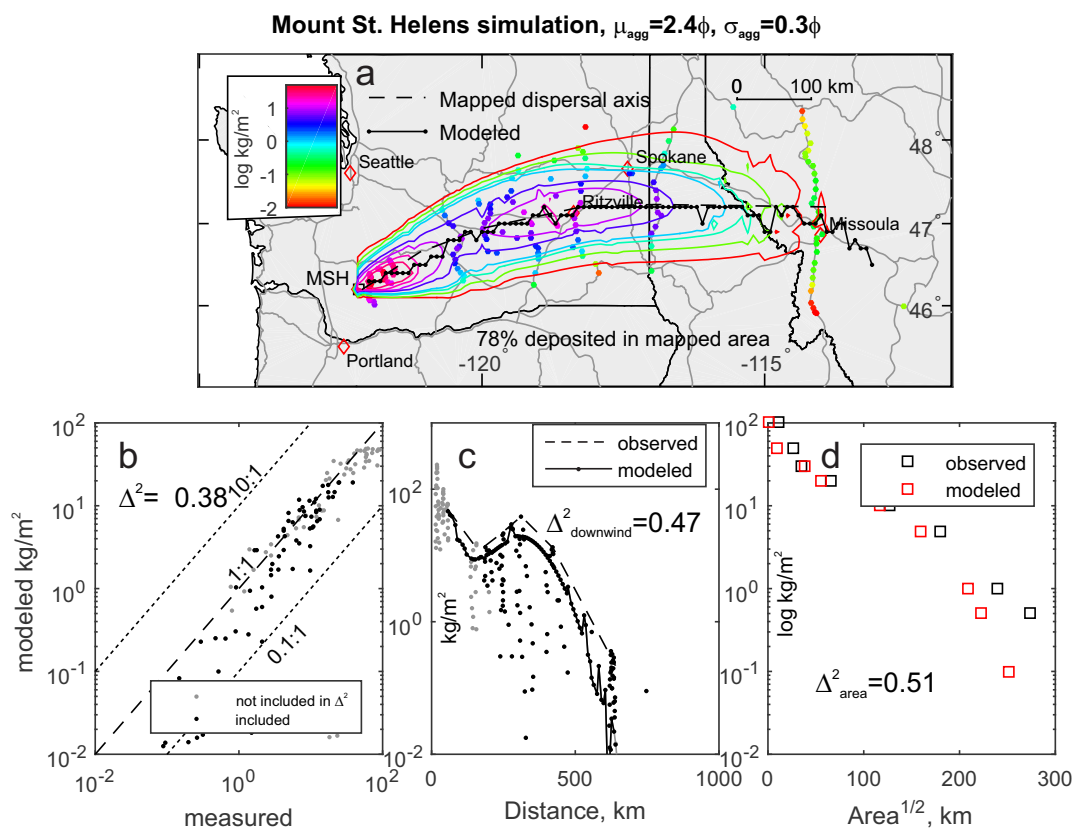


Figure 10

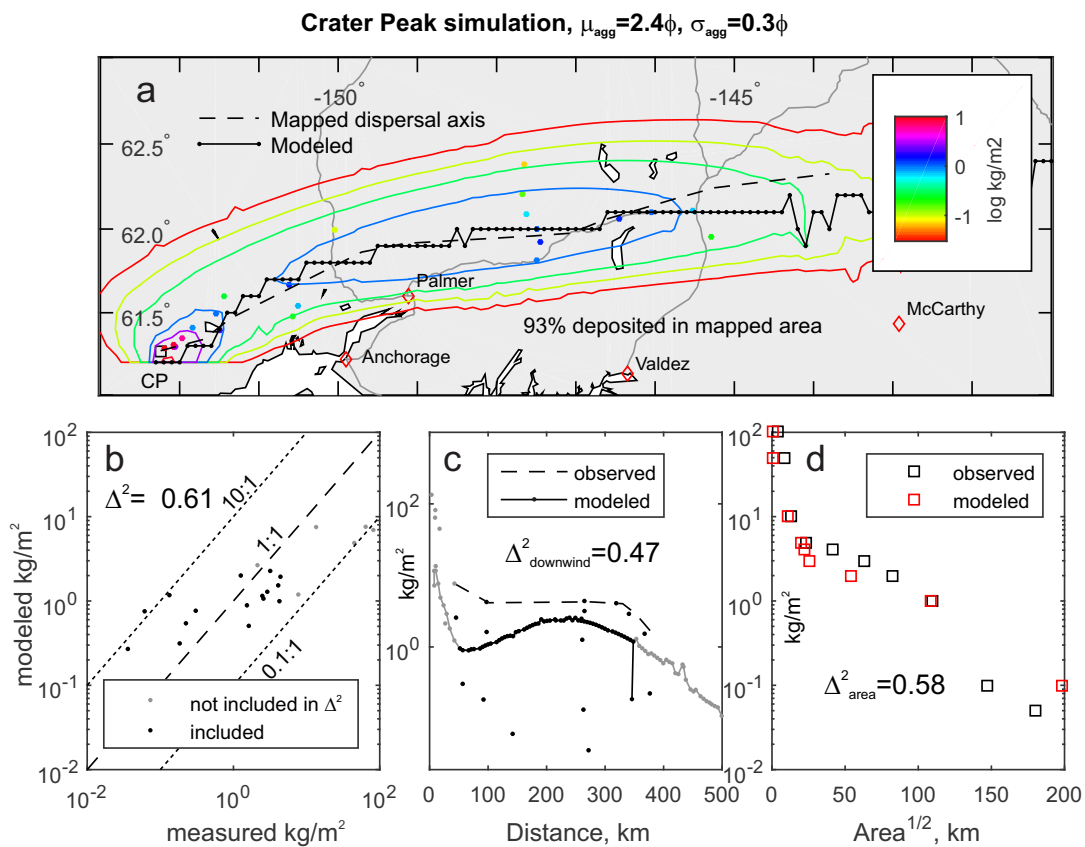


Figure 11

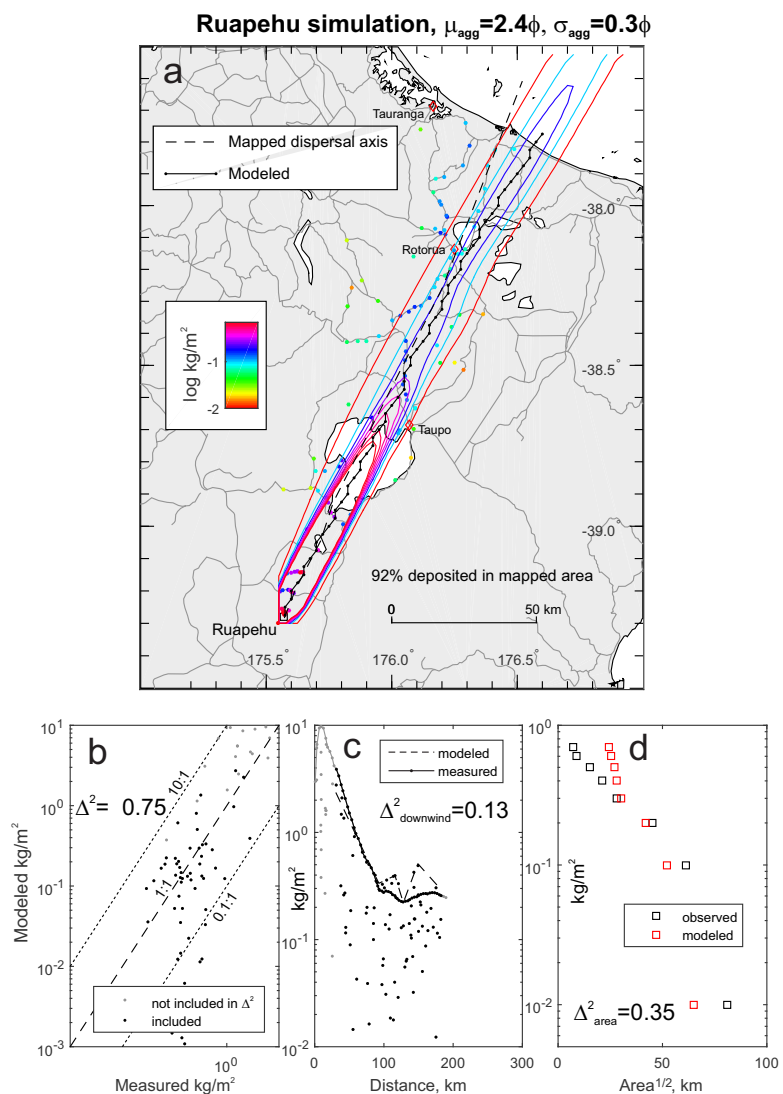


Figure 12



Redoubt simulation, $\mu_{agg}=2.4\phi$, $\sigma_{agg}=0.3\phi$

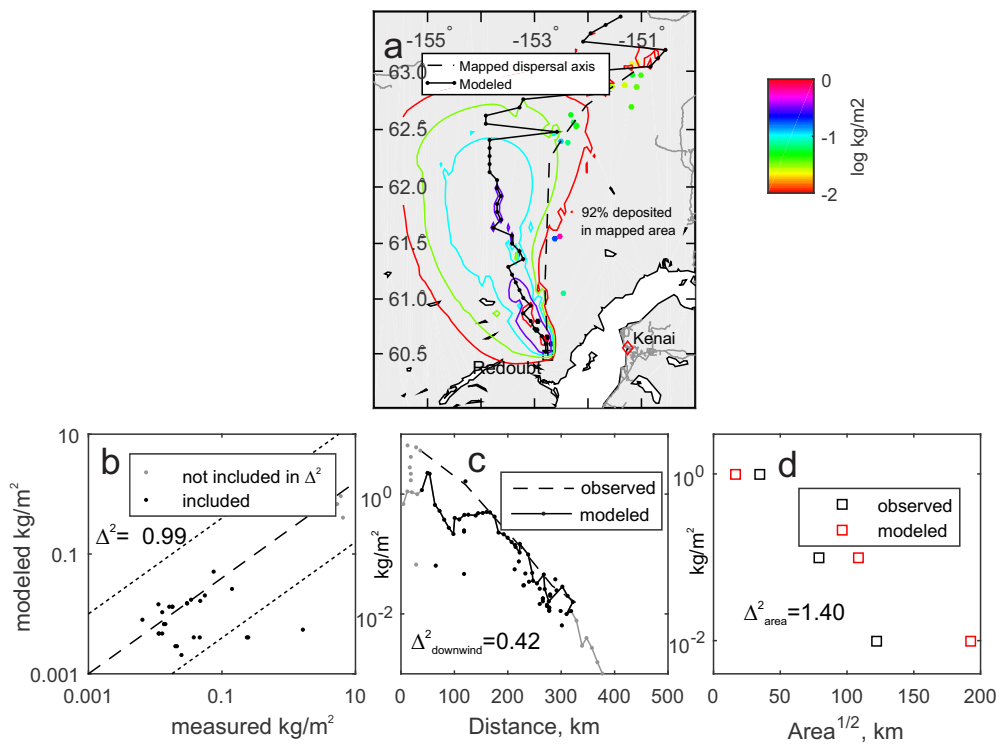


Figure 13

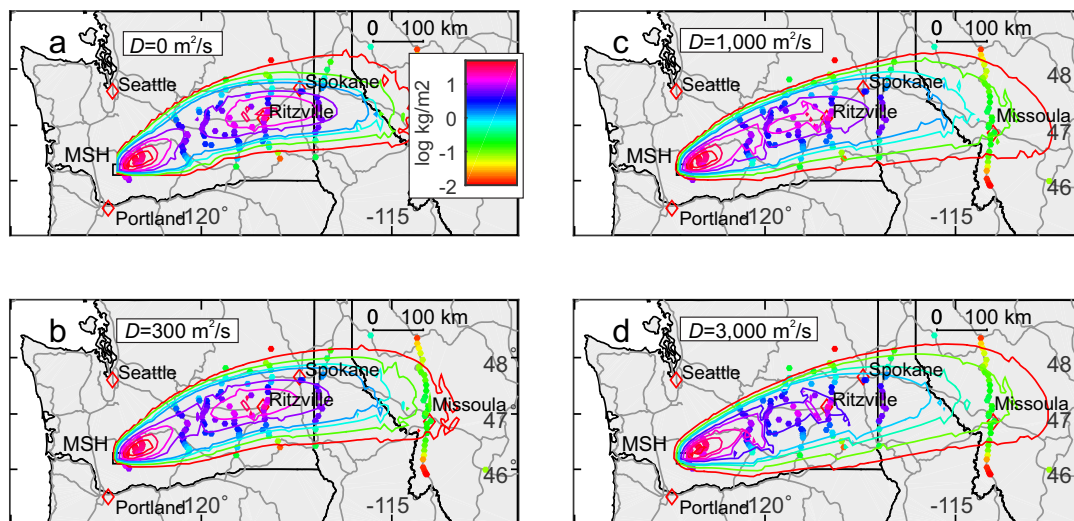


Figure 14

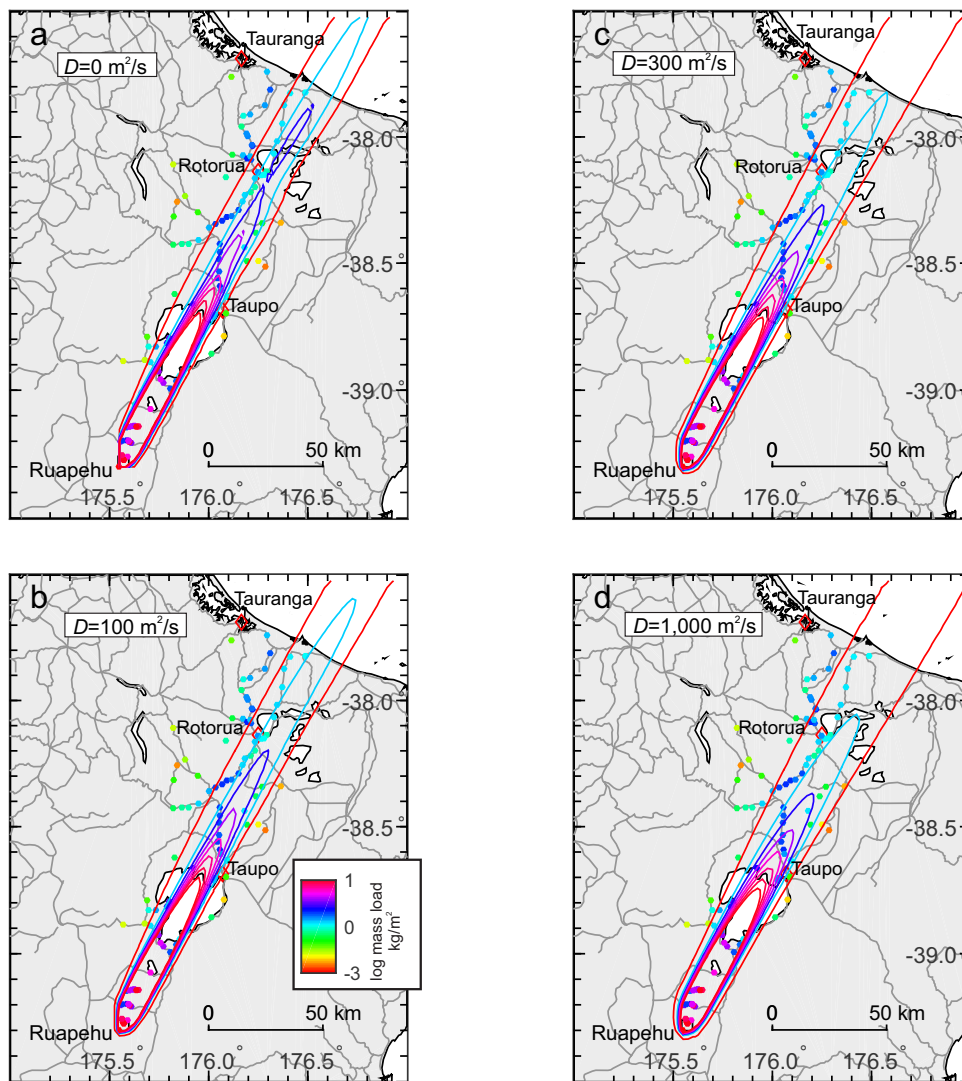


Figure 15

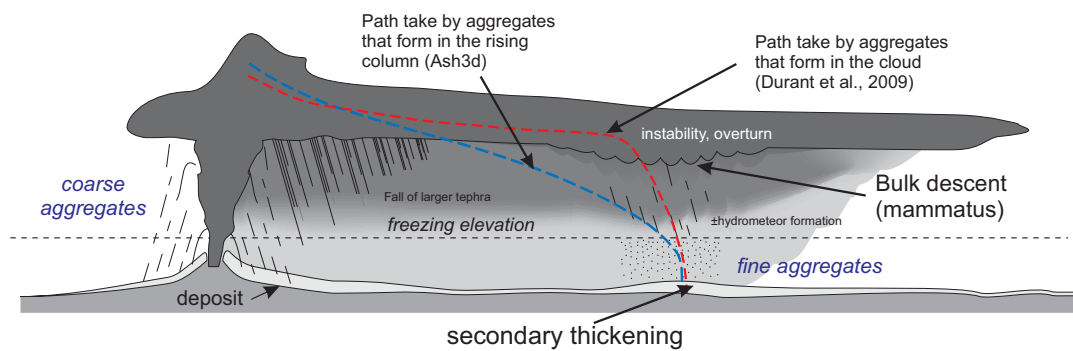


Figure A1